Chemical Geology 644 (2024) 121840

Contents lists available at ScienceDirect

Chemical Geology

journal homepage: www.elsevier.com/locate/chemgeo

Deep segregation and crystallization of ultra-depleted melts in the sub-ridge mantle

C. Ferrando [a,b,*], G. Borghini [c], C. Sani [a], F. Genske [d], M. Ligi [e], A. Stracke [d], A. Sanfilippo [a,f]

[a] Department of Earth and Environmental Sciences, University of Pavia, 27100 Pavia, Italy
[b] Department of Earth, Environmental and Life Sciences, University of Genova, 16132 Genova, Italy
[c] Department of Earth Sciences "Ardito Desio", University of Milano, 20133 Milano, Italy
[d] Institut für Mineralogie, Universität Münster, Germany
[e] National Research Council (CNR) - ISMAR, Bologna, Italy
[f] National Research Council (CNR) - IGG, Pavia, Italy

ARTICLE INFO

Editor: S Aulbach

Keywords:
Pyroxenites
Plagioclase-facies recrystallization
Hf-Nd isotopes
Doldrums Fracture Zone

ABSTRACT

Partial melting of mantle peridotite from which considerable amounts of melt have been extracted during prior melting episodes generates melts characterized by low incompatible element contents and very low ratios of highly to moderately incompatible elements, so-called 'ultra-depleted' melts. Reaction of peridotite with percolating ultra-depleted melts has been inferred from petrological-geochemical studies of abyssal peridotites and ophiolites. But so far, direct evidence for the existence of ultra-depleted melts, only comes from rare melt inclusions. Here, we show that a pyroxenite layer within abyssal peridotite from the Mid Atlantic Ridge (8°N, Doldrums Fracture Zone) formed by crystallization of a segregated melt that is highly depleted in incompatible elements, at >27 km-depth beneath the ridge axis (at T ~ 1250 °C), and with little or no modification by interaction with the host harzburgite. During exhumation, the pyroxenite experienced decompression and partial re-equilibration under plagioclase-facies conditions (~1060 °C and ~ 15 km depth). The high Hf isotope ratio (εHf = 40.3) of the pyroxenite clinopyroxene is inherited from a melt sourced from an ultra-depleted peridotite that evolved with high Lu/Hf. The associated MORB-like Nd isotope ratios (εNd = 10.6), however, imply a long-term evolution of the source peridotite with composition moderately depleted in incompatible elements (rather low Sm/Nd). These compositions are different from the host harzburgite, but typical for peridotites that have melted and partially reacted with migrating melts in ancient times. Hence, the pyroxenite investigated here is a partial melt from an ultra-depleted peridotite that has become re-enriched in incompatible elements and clinopyroxene. This melt crystallized in the oceanic lithosphere, and partially re-equilibrated at low pressure during exhumation. Overall, our results show that renewed melting of ultra-depleted peridotites with a complex history of prior melting and melt-rock reaction occurs, and that such melts migrate through the sub-ridge mantle, and can thus contribute to mid ocean ridge magmatism, although to a still unknown extent.

1. Introduction

The mass fluxes associated with continuous formation and recycling of oceanic crust into the deeper mantle control the chemical evolution of Earth's mantle. Oceanic crust generation leaves a compositionally heterogeneous residual peridotitic mantle, which is re-incorporated into the convective mantle flow, together with the overlying mafic crust via subduction dynamics. The two lithologies become intermingled, but do not re-homogenize (e.g., White, 1985; Stracke, 2012; Rampone and Hofmann, 2012; Tackley, 2015). The present mantle source of Mid-Ocean Ridge Basalts (MORBs) is therefore a heterogeneous assemblage of incompatible element depleted peridotites, formed during prior melting episodes some 10^8–10^9 years ago (e.g., Salters and Dick, 2002; Cipriani et al., 2004; Warren et al., 2009; Stracke et al., 2011; Shorttle et al., 2014; Warren, 2016; Sani et al., 2023), plus minor amounts of recycled oceanic crust and metasomatic veins (+/− other components, e.g., recycled continental crust; e.g., Guo et al., 2023 and reference therein).

The geochemical and isotopic variability of MORBs represents a muted picture of the heterogeneous mantle because primary melts from

* Corresponding author at: Dipartimento di Scienze della Terra, dell'Ambiente e della Vita, University of Genova, Corso Europa 26, 16132 Genova, Italy.
E-mail address: carlotta.ferrando@unige.it (C. Ferrando).

https://doi.org/10.1016/j.chemgeo.2023.121840
Received 30 August 2023; Received in revised form 17 November 2023; Accepted 18 November 2023
Available online 22 November 2023
0009-2541/© 2023 The Authors. Published by Elsevier B.V. This is an open access article under the CC BY license (http://creativecommons.org/licenses/by/4.0/).

the different individual mantle components aggregate prior to eruption (e.g., Stracke, 2012, 2021; Rudge et al., 2013; Sanfilippo et al., 2021). This ubiquitous melt mixing readily buffers the composition of the aggregated melt toward the most incompatible element enriched, or least depleted, mantle components. Thereby, it also effectively disguises the isotopic and elemental signatures of melts from peridotite domains with highly depleted incompatible element contents, and very low ratios of highly to moderately incompatible elements, so-called 'ultra-depleted' peridotites (e.g., Stracke and Bourdon, 2009; Warren et al., 2009; Salters et al., 2011; Stracke, 2012; Rudge et al., 2013; Liu and Liang, 2017; Stracke et al., 2019; Borghini et al., 2021). As a result, the Nd—Hf isotope ratios of melts erupted at ocean ridges vary within a relatively narrow range (Fig. 1); they lack the very high Hf and Nd isotope ratios expected for partial melting of ultra-depleted peridotite domains (Salters et al., 2011; Sanfilippo et al., 2019; Stracke, 2021).

Moreover, most Nd—Hf isotope ratios of mantle peridotites sampled along mid-ocean ridges overlap the range of MORBs (Fig. 1). Much higher Hf isotope ratios in clinopyroxenes from abyssal peridotites (Gakkel Ridge, Stracke et al., 2011; Mid Atlantic Ridge, Sani et al., 2023) and ophiolite massifs (Blichert-Toft et al., 1999; Guarnieri et al., 2012; Sanfilippo et al., 2019; Liu et al., 2020), and Hawaiian xenoliths, Salters and Zindler, 1995; Bizimis et al., 2003; Fig. 1), however, indicate that ultra-depleted peridotite domains existed in the mantle for some 10^8–10^9 years prior to recent melting (e.g., Salters and Dick, 2002; Bizimis et al., 2003; Cipriani et al., 2004; Warren et al., 2009; Stracke et al., 2011; Rampone and Hofmann, 2012; Byerly and Lassiter, 2014; Mallick et al., 2014; Tilhac et al., 2022). The isotopic composition of such refractory mantle domains extends far beyond the field of erupted MORBs (Fig. 1) and contributes to the dispersion of Hf—Nd isotope ratios observed in global MORBs (Salters et al., 2011; Sanfilippo et al., 2019, 2021).

Olivine-hosted melt inclusions with ultra-depleted trace element compositions (Sobolev and Shimitzu, 1993) and Nd isotope ratios greater than those in MORBs (Stracke et al., 2019) also provide rare evidence that renewed partial melting of ultra-depleted peridotite domains can contribute to the geochemical diversity of oceanic basalts. Hints for the existence of melts from such ultra-depleted peridotites have also been found in dunites in ophiolites (Sanfilippo et al., 2019), pyroxenites from the Hawaiian plume (Bizimis et al., 2005), continental xenoliths (Byerly and Lassiter, 2014) and supra-subduction zone peridotites (Tilhac et al., 2020) and pyroxenites (Zhang et al., 2022). Moreover, pyroxenite layers in abyssal peridotites sampled along Mid-Ocean Ridges (see Warren, 2016 and references therein) probably are deep segregations of melts from ultra-depleted peridotite (e.g. Juteau et al., 1990; Kempton and Stephens, 1997; Dantas et al., 2007; Laukert et al., 2014; Basch et al., 2019). So far, however, Nd—Hf isotope data on these depleted abyssal pyroxenites have not been reported. Hence it remains unknown if their incompatible element depleted character is a product of extensive recent melting of a relatively incompatible-element-rich mantle or if it is inherited from re-melting ancient ultra-depleted peridotite. Because abyssal pyroxenites are commonly interpreted as crystallization products of melts segregated in the oceanic lithosphere (Dantas et al., 2007; Warren, 2016), their composition mirrors that of the parental-primary melts whose isotopic signature can reveal insights on the nature of the asthenospheric mantle.

Here, we report the first Nd—Hf isotope ratios measured on a pyroxenite vein within a harzburgite from the Doldrums Fracture Zone (FZ) (7°-8°N, Mid-Atlantic Ridge; Skolotnev et al., 2020). High Hf isotope ratios of peridotites from this section of the Equatorial Atlantic Ridge document the occurrence of ancient (>1.5 Ga) ultra-depleted peridotite domains, which were formed by partial melting 10^8–10^9 years ago but became re-enriched in incompatible elements and clinopyroxene by concomitant melt-rock reaction (Sani et al., 2023). In this study, we compare the geochemical and isotopic signatures of the pyroxenite vein (and its constituent minerals) with those of the host peridotite. In addition, we report Nd—Hf isotope data of nearby peridotites that show evidence for diffuse migration and crystallization of depleted melts at plagioclase-facies conditions (hereafter referred to as '*Pl-impregnated peridotite*' as classified by Sani et al., 2020), thus providing insights into the nature of the mantle source of such melts. We show that renewed melting of ultra-depleted peridotites with a complex history of prior melting and melt-rock reaction occurred. These melts migrated through the lithospheric mantle at Doldrums FZ and crystallized either in pyroxenite veins or interstitially within the peridotitic matrix, which formed the *Pl-impregnated peridotites*. The occurrence of ultra-depleted melts further implies that they can contribute to Mid-Ocean Ridge magmatism, although to a still unknown extent.

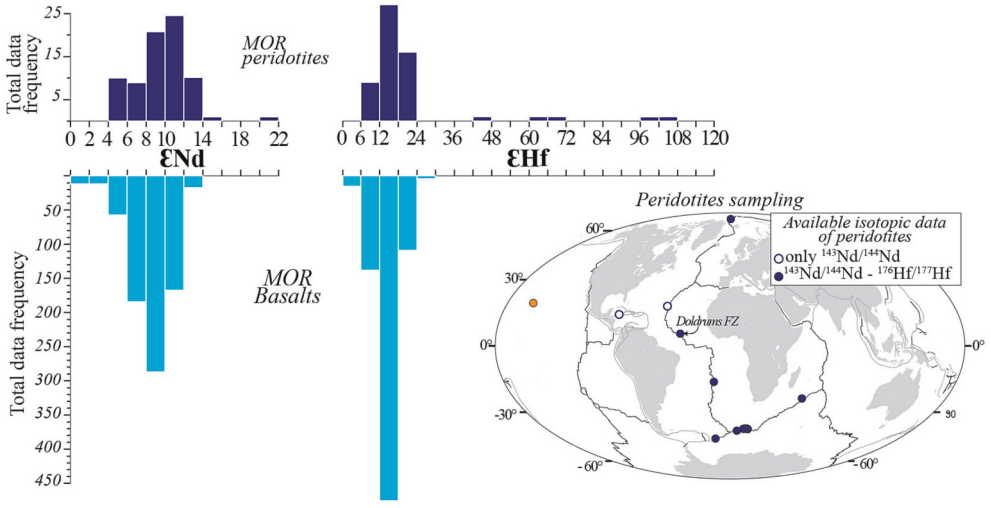

Fig. 1. Histograms showing the distribution of Nd and Hf isotope data of MORBs (Stracke, 2012; upside down, light blue colored) and mantle peridotites from mid-ocean ridges (SouthWest Indian Ridge – SWIR, Mid-Cayman Rise – MCR, Mid-Atlantic Ridge – MAR, Gakkel Ridge; Snow, 1993; Snow et al., 1994; Salters and Zindler, 1995; Salters and Dick, 2002; Cipriani et al., 2004; Warren et al., 2009; Stracke et al., 2011; Mallick et al., 2014, 2015; Frisby et al., 2016). On the Earth's map (redrawn after Warren, 2016) locations of abyssal peridotites analyzed for Hf—Nd isotopic (full dots = Nd-Hf isotopic compositions available; empty dots = only Nd isotopic data available) data are reported. (For interpretation of the references to colour in this figure legend, the reader is referred to the web version of this article.)

2. Abyssal peridotites from the Doldrums Fracture Zone, Mid Atlantic Ridge

The Doldrums Fracture Zone (Doldrums FZ) is one of the major discontinuities in the Equatorial Mid-Atlantic Ridge (MAR), characterized by a 630-km-long and 110-km-wide lens-shaped transform zone between 7°N and 8°N (Skolotnev et al., 2020). This complex system includes four intra-transform spreading ridges delimited by five active transform faults. The longest ridge offsets are observed in the northern sector at the so-called Doldrums (177 km-long active fault) and

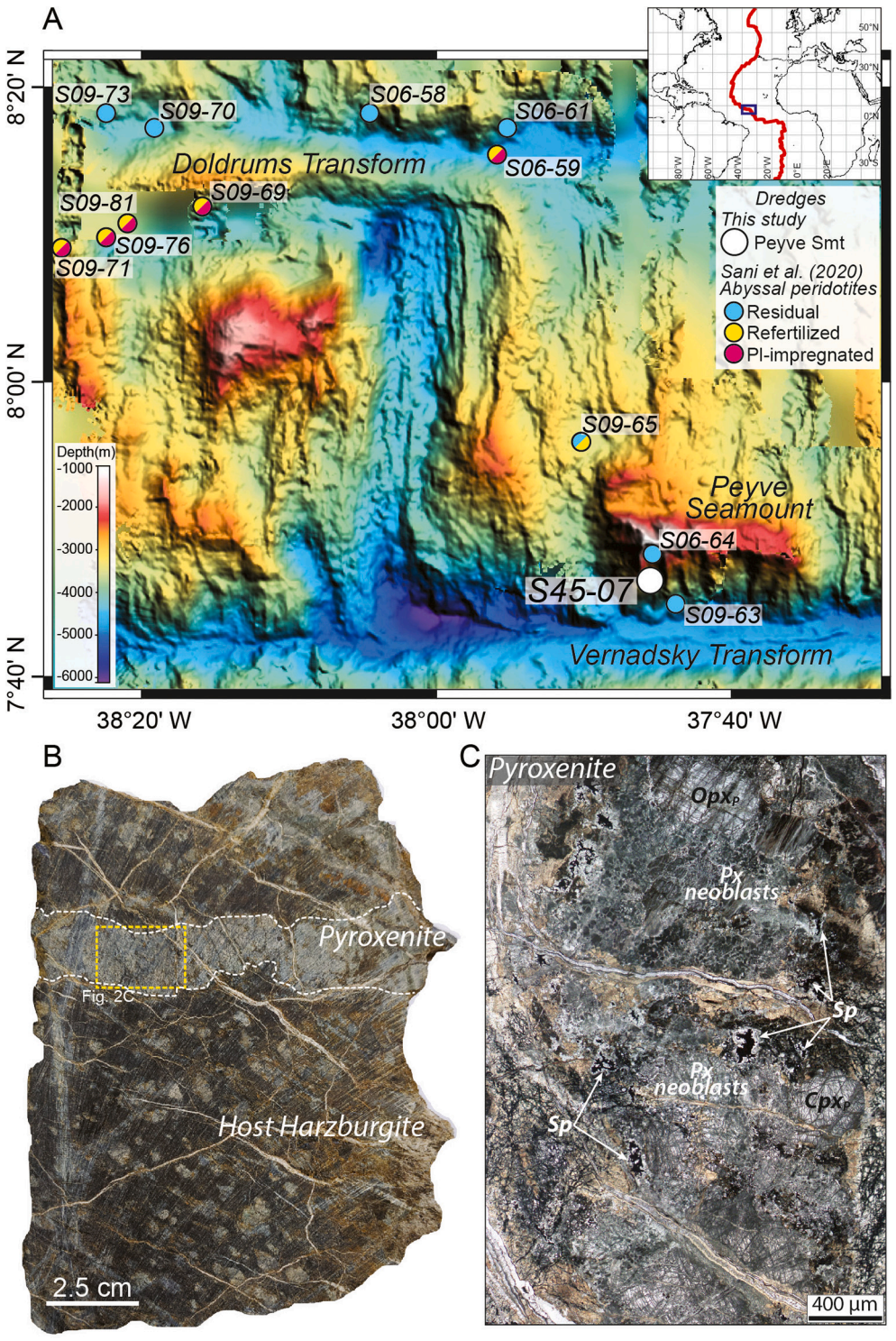

Fig. 2. A) Bathymetric map of the Mid-Atlantic Ridge between the Doldrums Transform and the Vernadsky Transform within the Doldrums Fracture Zone (see complete bathymetric map of the Doldrums Fracture Zone in Skolotnev et al., 2020). Dots indicate the dredges' locations, and their colours indicate the type of mantle peridotite sampled based on the classification by Sani et al., 2020. B) Occurrence of a pyroxenite vein within the host residual harzburgite from the Peyve Seamount; note the irregular but sharp contact between the pyroxenite and its host. The yellow box locates the thin section in (C). C) Thin section scan of the pyroxenite vein; large orthopyroxene and clinopyroxene porphyroclasts (Opx_P and Cpx_P, respectively) are mantled by abundant pyroxene (Px) neoblasts. Abundant spinel shows amoeboid shapes with plagioclase coronas. (For interpretation of the references to colour in this figure legend, the reader is referred to the web version of this article.)

the Vernadsky Transforms (145 km-long active fault) where gabbros and peridotites are exposed. Abyssal peridotites were dredged during three expeditions of the *R/V Akademik Nikolai Strakhov* (S06 and S09, Pushcharovsky et al., 1992; S45, Skolotnev et al., 2020) along the northern and southern walls of the Doldrums Transform and at the so-called Peyve Seamount, a near-axis transverse ridge on the northern wall of the Vernadsky Transform (Skolotnev et al., 2020; Fig. 2a). Based on textural features and mineral chemistry, Sani et al. (2020) grouped the recovered peridotites into three types: *residual peridotites*, *refertilized peridotites* and *Pl-impregnated peridotites*.

The *residual peridotites* are mainly sampled on the northern wall of the Doldrums Transform and on the Peyve Seamount (Fig. 2a). They lack any textural evidence for reaction with migrating melts during recent melting beneath the Mid Atlantic Ridge. The high Cr# and low TiO_2 contents (< 0.1 wt%) in spinels depict the residual character of these peridotites, suggesting average degrees of melting between 10% and 14% (Sani et al., 2020). The clinopyroxenes in these peridotites have remarkably low Zr, Hf and light REE (LREE) concentrations, but MORB-like Hf—Nd isotope ratios ($^{143}Nd/^{144}Nd$ = 0.51301 to 0.51328 and $^{176}Hf/^{177}Hf$ = 0.28312 to 0.28328). As discussed in detail in Sani et al. (2023), these combined trace element and isotopic compositions probably result from ancient partial melting and extensive melt-rock interaction, leading to moderately radiogenic present-day Hf—Nd isotope ratios, followed by recent melting at the Mid-Atlantic Ridge, which causes their pronounced incompatible element depletion.

Refertilized and *Pl-impregnated peridotites* were dredged on the southern wall of the Doldrums FZ and on a detachment fault on the eastern flank of the intra-transform spreading ridge (Fig. 2a). The *refertilized peridotites* are also incompatible element depleted but contain intergranular fine-grained clinopyroxenes with subtle enrichments in Na- and light REE. These features suggest entrapment and crystallization of melts at low melt-rock ratios and decreasing porosity (Sani et al., 2020). The clinopyroxenes in the *refertilized peridotites* have MORB-like Nd isotopic ratios ($^{143}Nd/^{144}Nd$ = 0.5130–0.5133), but show variably high $^{176}Hf/^{177}Hf$ (0.2841–0.2856). Sani et al. (2023) showed that these Hf—Nd isotope signatures are caused by interaction between an ancient, ultra-depleted peridotite and MORB-like melts. The very high Hf isotope ratios require that these peridotites evolved with ultra-depleted compositions prior to recent melting, and that the Hf isotopic ratios were only partially reset by melt-rock interaction, either during recent melting under the Mid Atlantic Ridge or in the past, or both (Sani et al., 2023).

The *Pl-impregnated peridotites* contain veins of plagioclase and orthopyroxene attesting to extensive migration (i.e., at high porosity conditions) of silica saturated melts through, and reaction with, the peridotite matrix. The high TiO_2 contents in spinel and the high middle and heavy REE concentrations in clinopyroxenes result from interactions at high melt-rock ratio. This reaction triggered complete re-equilibration of the mantle peridotitic matrix with the migrating melts and subsequent crystallization of the reacted melts as plagioclase-orthopyroxene veins. Previous models suggested that the light REE depletion in the clinopyroxenes requires that the reacting melts must have been highly depleted in incompatible elements (Sani et al., 2020).

3. Sample selection and analytical methods

In this study we investigated one pyroxenite vein and its associated host rock, a harzburgite (sample S45–07/107) from dredge S45–07 deployed on the southern slope of the Peyve Seamount. Although pyroxenites are globally ubiquitous, they constitute <5% of the total lithologies recovered at submarine mantle exposures (Warren, 2016). In addition to pyroxenites recovered along the Southwest Indian Ridge (Dantas et al., 2007; Warren et al., 2009) and at Lena Trough (Laukert et al., 2014), the pyroxenite vein from the Doldrums FZ represents one of the few abyssal pyroxenites analyzed to date. In addition, we also selected one *Pl-impregnated peridotite* (sample S09–71/01; dredge S09–71) from the southern wall of the Doldrums Transform (Expeditions S45 and S09 of the R/V Akademik Nikolaj Strakhov; Fig. 2a) believed to be formed by melt-rock interactions and re-equilibration with migrating melts (Sani et al., 2020; see previous section), thus in turn providing insights on the nature of the melts' mantle source.

The investigated pyroxenite vein is ~1–2 cm thick, with anastomosing and sharp contacts with the host peridotite (Fig. 2b). We determined mineral major (spinel, clinopyroxene, orthopyroxene and plagioclase) and trace element (clinopyroxene and orthopyroxene) concentrations of minerals from the pyroxenite, and from the host peridotite at the pyroxenite-peridotite contact, as well as ~6 cm away from the contact (Supplementary Fig. S1). We analyzed core- and rim-crystals of porphyroclasts and neoblasts. In addition, areal analyses of ~50 × 50 μm-size were performed on the cores of exsolved pyroxene porphyroclasts and neoblasts, with the aim to reconstruct the original compositions prior to cooling.

The *Pl-impregnated peridotite* was previously analyzed by Sani et al. (2020), who also provide a detailed textural description of this sample (S09–71/01 see also section 2 'Abyssal peridotites from the Doldrums Fracture Zone, Mid Atlantic Ridge').

Mineral major element compositions of the pyroxenite and host peridotite were analyzed in this study and are reported in Supplementary Table S1. The orthopyroxene and clinopyroxene trace element compositions and Nd—Hf isotope ratios of clinopyroxene separates from all studied samples are listed in Table 1.

Major element composition of minerals (spinel, olivine and pyroxenes) and X-ray element maps of Ca, Mg, Fe, Al, Cr, Na and Si were obtained using the Electron Probe MicroAnalyzer (EPMA) JEOL JXA8200 Super Probe operating at the University of Milan (Italy). An accelerating voltage of 15 kV was applied for all analyses. All minerals were measured with a beam current of 15 nA and 1 μm beam size. Counting time was 30 s for peak and 10 s for background.

In situ trace element composition of clinopyroxenes were determined using the Inductively Coupled Plasma Mass Spectrometry using a QQQ-ICP-MS Agilent Series 8900 interfaced to a GeoLas 193 nm excimer ablation system (Lambda Physik, Germany) at the CNR–IGG S.S. of Pavia. The ablation system was operated at a 10 Hz frequency with a fluence of about 9 J/cm^2 and spot diameter typically of 50–75 μm. Helium was used as carrier gas and mixed with Ar downstream of the ablation cell. Data reduction was performed using the software package GLITTER®51 (Griffin et al., 2008) and concentrations were calibrated against NIST SRM 610 synthetic glass (Jochum et al., 2011), whereas ^{44}Ca was used for internal standardization based on EPMA data. Precision and accuracy were assessed from repeated analyses of BCR-2 reference material and were better than ±10% (1SD).

Isotope measurements of clinopyroxene, leaching, dissolution and column chemistry were done at the Institut für Mineralogie, Universität Münster. The clinopyroxene separates (~150 mg to yield at least 5–10 ng of Hf and Nd according to previously determined trace element concentrations via LA-ICP-MS, hand-picked under binocular microscope) were leached with H_2O_2 and, subsequently, in 6 N HCl in an ultrasonic bath, followed by leaching in 6 N HCl at 100 °C to remove the effects of seawater alteration. The grains were initially dissolved in a mixture of concentrated HF:HNO_3 (4:1) for 3 days at 140 °C. After drying (120 °C), the samples were re-dissolved in 6 N HCl together with H_3BO_3 at 120 °C to avoid the formation of insoluble fluorides. These fully dissolved samples were subsequently dried down once more at 120 °C. After dissolution, Sr, high field strength element (HFSE) and rare earth element (REE) fractions of the samples were separated on a standard cation exchange column (resin Biorad® AG50W-X8, mesh size 200–400 μm). Hafnium was further purified from the HFSE fraction and Neodymium from the REE fraction using Eichrom® Ln Spec resin. The Nd and Hf isotope ratios were determined on 10 to 20 ng/g solutions using a Thermo Scientific NEPTUNE *Plus* MC-ICP-MS. Repeated measurements of the JMC-475 Hf standard gave an average $^{176}Hf/^{177}Hf = 0.282160 \pm 13$ (2 S.D., $n = 8$, 10–30 ng/g Hf solutions). All Hf isotope ratios are reported relative to $^{176}Hf/^{177}Hf = 0.282160$ (Blichert-

Table 1
Trace element compositions of clinopyroxenes (Cpx) and Orthopyroxenes (Opx) and Nd—Hf isotopic compositions of clinopyroxene in the Pyroxenite and its Host harzburgite and in the Pl impregnated peridotite.

Lithology	*Pyroxenite S45–7/107*																					
Phase	Cpx		Cpx		Cpx		Cpx		Opx		Opx		Opx		Opx		Opx		Opx		Opx	
Site	porph. Core		neob. Core		neob. Core		neob. Core		porph. Core		porph. Core		porph. Core		porph. Core		porph. Core		porph. Core		porph. Core	
ppm	*avg. (2 pt.)*	*St. Dev.*	*avg. (2 pt.)*	*St. Dev.*	*avg. (2 pt.)*	*St. Dev.*	*avg. (2 pt.)*	*St. Dev.*	*avg. (2 pt.)*	*St. Dev.*	*avg. (3 pt.)*	*St. Dev.*	*avg. (2 pt.)*	*St. Dev.*	*avg. (2 pt.)*	*St. Dev.*	*avg. (2 pt.)*	*St. Dev.*	*avg. (2 pt.)*	*St. Dev.*	*avg. (2 pt.)*	*St. Dev.*
Sc	53.11	1.82	54.03	15.93	58.45	4.63	60.91	1.22	30.18	1.61	30.61	2.50	35.81	6.17	29.91	0.37	32.95	0.54	32.23	2.04	38.39	0.30
Ti	1115	72	937	353	996	40	1128	4	420	25	417	28	378	9	416	0.5	428	7	604	1.5	407	0.7
V	319	14	283	89	296	6	304	18	165	0	159	2	166	15	183	1	174	4	185	7	190	5
Cr	9290	104	7153	1986	8142	238	7930	36	5865	153	5352	302	4558	73	6920	105	6011	13	6444	196	5940	207
Co	25.41	0.59	31.88	15.12	24.05	0.78	23.28	0.23	57.47	2.13	56.58	2.26	51.71	1.26	63.51	2.33	61.59	0.35	61.59	0.89	61.08	0.16
Ni	413	22	450	147	368	3	352	0	733	0	703	26	651	14	861	22	806	9	824	7	795	0.8
Zn	13.55	1.97	16.30	12.07	11.95	2.14	10.10	0.49	39.50	2.30	36.49	1.39	39.06	5.08	39.78	2.00	37.28	2.02	38.00	0.08	38.78	0.86
Rb	0.164	0.006	0.081	0.026	0.078	0.033	0.060	–	0.082	0.047	0.153	–	0.099	–	b.d.l.	–	0.029	–	0.234	–	0.038	–
Sr	1.351	0.137	0.393	0.228	0.391	0.288	0.270	0.038	0.212	0.112	0.421	0.553	0.094	–	0.064	–	0.036	–	0.850	1.150	0.036	–
Y	10.415	0.375	8.365	4.815	11.305	1.506	12.825	0.290	1.505	0.054	1.494	0.216	2.136	0.840	1.310	0.001	1.299	0.125	1.344	0.233	1.900	0.042
Zr	0.332	0.071	0.286	0.101	0.437	0.107	0.396	0.082	0.145	–	0.091	0.037	0.101	0.035	0.074	–	0.071	–	0.059	0.001	0.057	0.001
Nb	0.033	0.007	0.021	–	0.051	–	b.d.l.	–	0.077	0.007	0.031	–	0.026	0.011	b.d.l.	–	0.027	–	0.031	0.009	0.025	–
Ba	0.735	0.267	0.138	0.047	0.135	0.154	0.073	0.058	0.086	0.023	0.183	–	b.d.l.	–	0.028	0.027	0.031	–	0.489	–	0.051	–
La	b.d.l.	–	0.021	0.025	b.d.l.	–	0.020	–	0.057	–	0.012	–	0.040	–	0.011	–	b.d.l.	–	0.010	–	b.d.l.	–
Ce	0.035	0.012	0.045	0.028	0.038	0.021	b.d.l.	–	0.069	0.010	0.018	–	b.d.l.	–	0.022	–	0.009	–	0.038	–	0.021	–
Pr	0.017	–	0.024	0.011	0.044	0.026	b.d.l.	–	0.106	–	b.d.l.	–	b.d.l.	–	b.d.l.	–	b.d.l.	–	b.d.l.	–	b.d.l.	–
Nd	0.255	0.063	0.263	0.157	0.328	0.021	0.273	0.013	b.d.l.	–	0.140	–	b.d.l.	–	0.031	–	0.074	–	b.d.l.	–	0.063	–
Sm	0.217	0.008	0.250	0.085	0.393	0.105	0.445	0.007	b.d.l.	–	b.d.l.	–	0.143	–	b.d.l.	–	0.091	–	0.108	–	b.d.l.	–
Eu	0.190	0.098	0.142	0.049	0.164	0.046	0.208	0.038	b.d.l.	–	b.d.l.	–	0.045	–	b.d.l.	–	b.d.l.	–	b.d.l.	–	b.d.l.	–
Gd	0.950	0.071	0.815	0.474	1.140	0.127	1.115	0.148	0.144	–	b.d.l.	–	0.156	–	b.d.l.	–	0.177	–	b.d.l.	–	0.051	–
Tb	0.175	0.018	0.233	0.052	0.276	0.006	0.348	0.021	0.029	–	0.026	–	0.022	–	0.026	–	0.025	0.013	0.027	0.015	0.027	0.017
Dy	1.720	0.184	1.418	0.854	1.965	0.092	2.660	0.000	0.300	0.004	0.221	0.034	0.314	0.068	0.128	0.022	0.153	0.073	0.188	0.074	0.208	0.071
Ho	0.438	0.046	0.323	0.193	0.453	0.018	0.574	0.006	0.107	0.009	0.045	0.017	0.067	0.032	0.042	0.009	0.059	0.010	0.065	0.005	0.084	0.010
Er	1.075	0.035	0.978	0.533	1.132	0.117	1.293	0.018	0.295	0.209	0.193	0.121	0.235	0.018	0.133	0.002	0.263	0.035	0.190	0.037	0.249	0.054
Tm	0.162	0.030	0.146	0.089	0.230	0.017	0.233	0.079	0.062	0.021	0.052	–	0.032	0.016	0.023	0.002	0.048	0.003	0.042	0.019	0.042	0.001
Yb	1.445	0.148	0.961	0.470	1.515	0.148	1.265	0.134	0.295	0.064	0.289	0.060	0.430	0.120	0.234	0.089	0.289	0.017	0.310	0.100	0.361	0.025
Lu	0.147	0.004	0.162	0.080	0.194	0.076	0.218	0.016	0.088	0.006	0.058	0.014	0.062	0.006	0.030	0.012	0.041	0.022	0.076	0.024	0.092	0.001
Hf	0.111	0.065	0.156	0.132	0.122	0.025	0.154	0.061	0.086	–	b.d.l.	–	0.106	–	b.d.l.	–	b.d.l.	–	0.089	0.018	b.d.l.	–
Ta	0.014	–	0.008	–	0.021	–	0.026	–	0.068	0.068	0.010	–	b.d.l.	–	b.d.l.	–	b.d.l.	–	b.d.l.	–	b.d.l.	–
Pb	0.089	–	0.063	0.019	0.163	–	0.056	–	0.201	0.098	0.058	0.027	0.062	0.025	b.d.l.	–	b.d.l.	–	0.131	–	0.068	–
Th	0.005	–	0.088	0.059	0.079	–	0.020	–	0.126	–	0.031	–	0.008	–	b.d.l.	–	0.013	–	b.d.l.	–	b.d.l.	–
U	0.013	–	0.017	0.013	0.063	–	0.022	–	0.049	0.040	0.011	–	0.022	–	b.d.l.	–	0.018	–	0.010	0.002	b.d.l.	–
147Sm/ 144Nd	0.515		0.575		0.724		0.986															

Lithology	*Pyroxenite S45–7/107*																					
Phase	Opx		Opx		Opx		Opx		Opx		Opx		Opx		Opx		Opx		Opx		Opx	
Site	porph. Core		porph. Core		porph. Core		porph. Core		porph. Core		porph. Core		porph. Core		porph. Core		porph. Core		porph. Core		neob. Core	
ppm	*avg. (2 pt.)*	*St. Dev.*	*avg. (2 pt.)*	*St. Dev.*	*avg. (2 pt.)*	*St. Dev.*	*avg. (2 pt.)*	*St. Dev.*	*avg. (2 pt.)*	*St. Dev.*	*avg. (2 pt.)*	*St. Dev.*	*avg. (2 pt.)*	*St. Dev.*	*avg. (2 pt.)*	*St. Dev.*	*avg. (2 pt.)*	*St. Dev.*	*avg. (2 pt.)*	*St. Dev.*	*1 pt.*	
Sc	32.95	0.54	32.23	2.04	38.39	0.30	31.70															
Ti	428	7	604	1.5	407	0.7	403															
V	174	4	185	7	190	5	165															
Cr	6011	13	6444	196	5940	207	5119															
Co	61.59	0.35	61.59	0.89	61.08	0.16	54.78															
Ni	806	9	824	7	795	0.8	652															
Zn	37.28	2.02	38.00	0.08	38.78	0.86	39.40															
Rb	0.029	–	0.234	–	0.038	–	0.081															
Sr	0.036	–	0.850	1.150	0.036	–	b.d.l.															
Y	1.299	0.125	1.344	0.233	1.900	0.042	1.486															
Zr	0.071	–	0.059	0.001	0.057	0.001	0.088															
Nb	0.027	–	0.031	0.009	0.025	–	b.d.l.															
Ba	0.031	–	0.489	–	0.051	–	b.d.l.															
La	b.d.l.	–	0.010	–	b.d.l.	–	b.d.l.															
Ce	0.009	–	0.038	–	0.021	–	0.024															
Pr	b.d.l.	–	b.d.l.	–	b.d.l.	–	b.d.l.															
Nd	0.074	–	b.d.l.	–	0.063	–	b.d.l.															
Sm	0.091	–	0.108	–	b.d.l.	–	b.d.l.															
Eu	b.d.l.	–	b.d.l.	–	b.d.l.	–	b.d.l.															
Gd	0.177	–	b.d.l.	–	0.051	–	b.d.l.															
Tb	0.025	0.013	0.027	0.015	0.027	0.017	0.024															
Dy	0.153	0.073	0.188	0.074	0.208	0.071	b.d.l.															
Ho	0.059	0.010	0.065	0.005	0.084	0.010	0.077															
Er	0.263	0.035	0.190	0.037	0.249	0.054	0.326															
Tm	0.048	0.003	0.042	0.019	0.042	0.001	b.d.l.															
Yb	0.289	0.017	0.310	0.100	0.361	0.025	0.326															
Lu	0.041	0.022	0.076	0.024	0.092	0.001	b.d.l.															
Hf	b.d.l.	–	0.089	0.018	b.d.l.	–	b.d.l.															
Ta	b.d.l.	–	b.d.l.	–	b.d.l.	–	b.d.l.															
Pb	b.d.l.	–	0.131	–	0.068	–	0.046															
Th	0.013	–	b.d.l.	–	b.d.l.	–	b.d.l.															
U	0.018	–	0.010	0.002	b.d.l.	–	0.025															
147Sm/ 144Nd																						

(*continued on next page*)

Table 1 (*continued*)

Lithology	*Pyroxenite S45–7/107*																					
Phase	Cpx		Cpx		Cpx		Cpx		Opx		Opx		Opx		Opx		Opx		Opx		Opx		Opx
Site	porph. Core		neob. Core		neob. Core		neob. Core		porph. Core		porph. Core		porph. Core		porph. Core		porph. Core		porph. Core		porph. Core		neob. Core
ppm	*avg. (2 pt.)*	*St. Dev.*	*avg. (2 pt.)*	*St. Dev.*	*avg. (2 pt.)*	*St. Dev.*	*avg. (2 pt.)*	*St. Dev.*	*avg. (2 pt.)*	*St. Dev.*	*avg. (3 pt.)*	*St. Dev.*	*avg. (2 pt.)*	*St. Dev.*	*avg. (2 pt.)*	*St. Dev.*	*avg. (2 pt.)*	*St. Dev.*	*avg. (2 pt.)*	*St. Dev.*	*avg. (2 pt.)*	*St. Dev.*	*1 pt.*
176Lu/177Hf	0.188		0.148		0.226		0.201																

Lithology	*Host Harzburgite S45–7/107*																				*Pl impregnated S09–71/01 (Sani et al. (2020)*	
Location in sample	*Pxite-Hrz contact*		*~6 cm from contact*		*~6 cm from contact*		*~6 cm from contact*		*~6 cm from contact*	*Pxite-Hrz contact*	*~6 cm from contact*		*~6 cm from contact*		*~6 cm from contact*		*~6 cm from contact*		*~6 cm from contact*			
Phase	Cpx		Cpx		Cpx		Cpx		Cpx	Opx	Opx		Opx		Opx		Opx		Opx		Cpx	
Site	porph. Core		porph. Core		porph. Core		neob. Core		neob. Core	porph. Core	porph. Core		porph. Core		porph. Core		neob. Core		neob. Core			
ppm	*avg. (3 pt.)*	*St.Dev.*	*avg. (3 pt.)*	*St.Dev.*	*avg. (2 pt.)*	*St.Dev.*	*avg. (2 pt.)*	*St. Dev.*	*1 pt.*	*1 pt.*	*avg. (2 pt.)*	*St. Dev.*	*avg. (2 pt.)*	*St. Dev.*	*1 pt.*	*avg. (2 pt.)*	*St. Dev.*	*avg. (2 pt.)*	*St. Dev.*			
Sc	45.86	2.40	60.13	5.08	56.55	1.63	49.54	0.15	51.44	28.63	28.90	0.93	28.88	1.91	27.78	30.47	1.71	29.98	0.95	67.84		
Ti	840	41	1170	103	1135	3	1071	85	1013	298	442	19	439	61	397	401	15	389	38	n.d.		
V	280	8	363	28	367	2	327	19	341	143	182	0.4	176	10	169	175	6	176	3	n.d.		
Cr	7975	239	11,426	893	11,745	70	8450	875	8004	4006	5884	184	5482	288	5348	4292	44	4484	270	8077		
Co	26.73	2.65	40.78	8.19	45.02	0.33	27.60	1.62	30.88	54.78	64.60	4.43	62.95	1.63	61.41	55.90	1.54	60.47	0.85	n.d.		
Ni	410	34	957	274	656	6	412	2	468	705	827	49	781	27	786	676	45	687	18	n.d.		
Zn	16.54	0.79	33.44	6.98	27.57	1.34	16.06	0.11	17.09	42.00	43.61	4.73	43.50	5.66	39.00	31.81	5.49	43.84	3.92	n.d.		
Rb	0.110	0.023	1.185	0.644	0.088	–	0.032	–	0.036	0.111	0.081	–	0.042	–	b.d.l.	0.617	–	0.046	0.002	n.d.		
Sr	0.358	0.192	2.258	0.841	0.217	0.080	0.205	0.010	0.516	0.450	0.043	0.043	b.d.l.	–	b.d.l.	0.036	–	0.096	0.010	1.131		
Y	7.487	0.367	7.277	0.272	7.405	0.191	6.380	0.509	6.750	1.087	1.040	0.148	1.175	0.153	1.090	0.819	0.050	0.868	0.067	23.178		
Zr	0.239	0.028	0.191	0.212	0.242	0.038	0.201	0.024	0.267	b.d.l.	0.068	0.065	0.041	–	0.080	0.058	–	0.084	–	6.199		
Nb	0.037	0.028	b.d.l.	–	b.d.l.	–	0.037	–	0.017	0.070	0.020	–	b.d.l.	–	b.d.l.	0.040	–	b.d.l.	–	n.d.		
Ba	0.127	0.093	0.892	0.379	0.040	0.019	0.037	–	0.159	0.100	0.158	–	0.017	–	b.d.l.	0.056	0.024	0.134	–	n.d.		
La	b.d.l.	–	0.058	0.027	b.d.l.	–	0.016	–	b.d.l.	b.d.l.	0.010	–	0.010	–	0.008	0.011	–	b.d.l.	–	0.088		
Ce	0.016	–	0.173	0.022	0.028	–	b.d.l.	–	0.025	0.035	b.d.l.	–	b.d.l.	–	b.d.l.	0.011	–	0.038	–	0.536		
Pr	b.d.l.	–	0.025	0.000	0.010	0.001	0.014	–	0.016	b.d.l.	b.d.l.	–	b.d.l.	–	b.d.l.	b.d.l.	–	b.d.l.	–	0.173		
Nd	0.191	0.032	0.210	0.011	0.200	0.077	0.118	0.053	0.150	b.d.l.	b.d.l.	–	0.115	–	b.d.l.	b.d.l.	–	0.028	–	1.804		
Sm	0.243	0.087	0.265	0.068	0.253	0.006	0.236	0.003	0.281	b.d.l.	b.d.l.	–	0.093	–	b.d.l.	b.d.l.	–	0.034	–	1.366		

(*continued on next page*)

Table 1 (*continued*)

Lithology	*Host Harzburgite S45–7/107*																		*Pl impregnated S09–71/01 (Sani et al. (2020)*
Location in sample	*Pxite-Hrz contact*		*~6 cm from contact*		*~6 cm from contact*		*~6 cm from contact*		*~6 cm from contact*	*Pxite-Hrz contact*	*~6 cm from contact*		*~6 cm from contact*		*~6 cm from contact*		*~6 cm from contact*		
Phase	Cpx		Cpx		Cpx		Cpx		Cpx	Opx	Opx		Opx		Opx		Opx		Cpx
Site	porph. Core		porph. Core		porph. Core		neob. Core		neob. Core	porph. Core	porph. Core		porph. Core		porph. Core		neob. Core		
ppm	*avg. (3 pt.)*	*St.Dev.*	*avg. (3 pt.)*	*St.Dev.*	*avg. (2 pt.)*	*St.Dev.*	*avg. (2 pt.)*	*St. Dev.*	*1 pt.*	*1 pt.*	*avg. (2 pt.)*	*St. Dev.*	*avg. (2 pt.)*	*St. Dev.*	*1 pt.*	*avg. (2 pt.)*	*St. Dev.*	*avg. (2 pt.)*	*St. Dev.*	
Eu	0.172	0.027	0.101	0.018	0.142	0.050	0.071	0.043	0.140	0.040	0.014	–	0.027	–	b.d.l.	b.d.l.	–	b.d.l.	–	0.455
Gd	0.582	0.079	0.550	0.122	0.742	0.153	0.500	0.030	0.850	b.d.l.	0.048	–	0.041	–	0.062	0.070	–	0.119	0.027	2.696
Tb	0.164	0.013	0.165	0.017	0.146	0.006	0.127	0.002	0.116	b.d.l.	0.017	–	0.023	0.013	0.018	0.027	–	0.011	0.002	0.578
Dy	1.316	0.143	1.280	0.548	1.350	0.368	1.115	0.007	1.090	0.159	0.183	0.088	0.147	0.053	0.077	0.100	0.032	0.183	–	4.019
Ho	0.309	0.010	0.290	0.019	0.320	0.059	0.237	0.047	0.293	0.056	0.063	0.002	0.047	0.004	b.d.l.	0.034	0.005	0.038	–	0.899
Er	0.840	0.121	1.013	0.283	0.865	0.281	0.667	0.144	0.856	0.159	0.259	0.029	0.213	0.023	0.102	0.109	0.018	0.181	0.011	2.484
Tm	0.115	0.016	0.152	0.034	0.173	0.021	0.101	0.006	0.157	0.022	0.034	0.008	0.032	0.004	0.021	0.021	–	b.d.l.	–	0.356
Yb	1.153	0.226	1.000	0.205	1.010	0.240	0.853	0.264	0.780	0.214	0.297	–	0.259	0.054	0.319	0.190	0.032	0.181	–	2.377
Lu	0.140	0.022	0.127	0.036	0.132	0.056	0.101	0.008	0.138	0.049	0.041	0.021	0.032	0.007	0.059	0.032	–	0.037	0.001	0.311
Hf	b.d.l.	–	0.081	–	0.113	0.083	b.d.l.	–	b.d.l.	b.d.l.	b.d.l.	–	0.027	0.007	0.099	b.d.l.	–	b.d.l.	–	0.492
Ta	0.013	–	b.d.l.	–	0.025	–	0.005	–	b.d.l.	b.d.l.	b.d.l.	–	0.017	0.008	b.d.l.	b.d.l.	–	b.d.l.	–	n.d.
Pb	0.133	0.037	0.079	0.019	0.044	–	0.015	–	0.133	0.109	b.d.l.	–	0.020	–	0.027	0.018	–	0.025	–	n.d.
Th	0.028	–	0.026	–	b.d.l.	–	b.d.l.	–	b.d.l.	0.018	b.d.l.	–	b.d.l.	–	b.d.l.	0.023	–	b.d.l.	–	n.d.
U	0.005	–	0.069	0.068	0.016	–	b.d.l.	–	b.d.l.	b.d.l.	b.d.l.	–	b.d.l.	–	b.d.l.	b.d.l.	–	b.d.l.	–	n.d.
147Sm/144Nd	0.741		0.763		0.765		1.209		1.133											0.458
176Lu/177Hf	–		0.219		0.163		–		–											0.090

Lithology	*Host pyroxenite*		*Pyroxenite*		*Pl impregnated*	
		2 S.E.		*2 S.E.*		*2 S.E.*
147Sm/144Nd	0.764		0.515		0.458	
143Nd/144Nd	0.51320	9.70E-06	0.51318	1.576E-05	0.51297	1.28E-05
ƐNd	10.9		10.6		6.56	
176Lu/ 177Hf	0.194		0.188		0.090	
176Hf/ 177Hf	0.28323	1.38E-05	0.28391	5.912E-05	0.28359	2.95E-05
ƐHf	16.0		40.3		28.86	

Toft et al., 1999). To verify accuracy and to demonstrate reproducibility of the isotope ratio measurements, multiple small aliquots (i.e., <10 mg to obtain Nd—Hf concentrations similar to the samples) of USGS rock reference materials BHVO-2 and BCR-2 were processed as unknowns and gave $^{176}Hf/^{177}Hf = 0.283096 \pm 25$ (2 S.D., $n = 12$) for BHVO-2 and $^{176}Hf/^{177}Hf = 0.282867 \pm 20$ (2 S.D., $n = 10$) for BCR-2. The JNdi-1 (20 ppb) Nd bracketing standard was determined at $^{143}Nd/^{144}Nd = 0.512067 \pm 11$ (2SD, $n = 7$), and all data are normalized to JNdi-1 $^{143}Nd/^{144}Nd = 0.512115$ (Tanaka et al., 2008). The USGS rock standard BHVO-2 gave $^{143}Nd/^{144}Nd = 0.512981 \pm 18$ (2 S.D., n = 8) and $^{143}Nd/^{144}Nd = 0.512641 \pm 12$ (2 S.D., $n = 5$) for BCR-2. Both Hf and Nd isotope values of the USGS rock standards agree well with literature values, i.e., preferred values from the GeoReM data base (Jochum et al., 2007), were BHVO-2 is listed with $^{176}Hf/^{177}Hf = 0.283082 \pm 133$ (S.D.) and with $^{143}Nd/^{144}Nd = 0.512979 \pm 14$ (S.D.), and BCR-2 is listed with $^{176}Hf/^{177}Hf = 0.282865 \pm 13$ (S.D.) and with $^{143}Nd/^{144}Nd = 0.512635 \pm 29$ (S.D.). Note that $^{147}Sm/^{144}Nd$ and $^{176}Lu/^{177}Hf$ of clinopyroxene were calculated from the in-situ LA-ICP-MS trace element concentrations using the equations $^{147}Sm/^{144}Nd = Sm/Nd*(0.15*144.24/(0.238*150.36))$ and $^{176}Lu/^{177}Hf = Lu/Hf*(0.0259*178.49/(0.186*174.967))$.

4. Results

4.1. Petrography and minerals major element compositions

The investigated *pyroxenite* vein is a websterite and consists of large clinopyroxene and orthopyroxene porphyroclasts with abundant spinel crystals (Fig. 2c) and minor olivine. Black to brownish Cr-spinels have amoeboid shapes showing coronas of unaltered plagioclase + olivine (Fig. 3a-b). The spinel Cr# and Mg# in the pyroxenite cover the whole range of spinels in mantle peridotites from the Doldrums FZ (Fig. 4a and Supplementary Table S1). Specifically, the Cr# (Cr# = [Cr/(Cr + Al)] mol%) are between 35.9 and 52.3 and increase with decreasing Mg# (Mg# = [Mg/(Mg + Fe^2)] mol% in the range 33.2–66.5) from spinel core to rim (Supplementary Table S1). Their TiO_2 contents are nearly constant ($TiO_2 < 0.3$ wt%) and similar to pyroxenites from Lena Trough (Laukert et al., 2014; Fig. 4b). They are, however, higher than in spinels from the residual peridotites (as classified by Warren, 2016) and distinct from high-Ti spinels in melt-modified peridotites and plagioclase pyroxenites (e.g., Warren, 2016; Basch et al., 2019; Fig. 4a-b). Pyroxene porphyroclasts in the pyroxenite vein from the Doldrums FZ display undulous extinction suggesting that the pyroxenite was affected by weak solid-state deformation (Fig. 3c). Similar to the associated spinels, the pyroxenes have low TiO_2 concentrations (<0.3 wt%) and remarkably low Na_2O (Na_2O = 0.06–0.23 wt%; Fig. 4c-d, Supplementary Table S1; Supplementary Fig. S1). Large pyroxene porphyroclasts are exsolved. The CaO contents in clinopyroxene determined with areal analyses (~50 × 50 μm-size) of porphyroclast cores are lower than those obtained by spot analyses, but the CaO contents in orthopyroxene determined with areal analyses are higher than those of the spot analyses (Supplementary Table S1). The areal Ca concentrations are consistent with the pyroxenes composition prior to exsolution development (see Fig. 3a and Fig. 3c). The crystal cores of clino- and orthopyroxenes have high Al_2O_3 contents (Al_2O_3 $_{Cpx\ core}$ = 5.59–6.98 wt% and Al_2O_3 $_{Opx\ core}$ = 4.28–5.74 wt%; Supplementary Table S1) and Mg# of ~90, similar to other abyssal pyroxenites (Laukert et al., 2014; Dantas et al., 2007) and pyroxenites from ophiolites (e.g., Basch et al., 2019) (Fig. 4d). Clinopyroxene porphyroclasts show core-to-rim decreasing Al_2O_3 (Al_2O_3 $_{rim}$ = 3.47–4.48 wt%; Fig. 4c-d) with increasing Mg# (on average Mg# $_{core}$ ~ 90.6 and Mg# $_{rim}$ ~ 91.7; Supplementary Table S1), whereas orthopyroxenes do not show chemical zoning. Medium-grained and well-equilibrated neoblastic assemblages of pyroxenes with small interstitial crystals of plagioclase are widely distributed throughout the pyroxenite, mantling large orthopyroxene porphyroclasts (Fig. 3a) or replacing the primary clinopyroxenes (Fig. 3b and Fig. 3d). Pyroxene neoblasts have lower Al_2O_3 and higher Cr_2O_3 and Mg# compared to porphyroclast cores (Supplementary Table S1). Clinopyroxene neoblasts display Ca core-to-rim normal zonation (see Fig. 3d) and decreasing

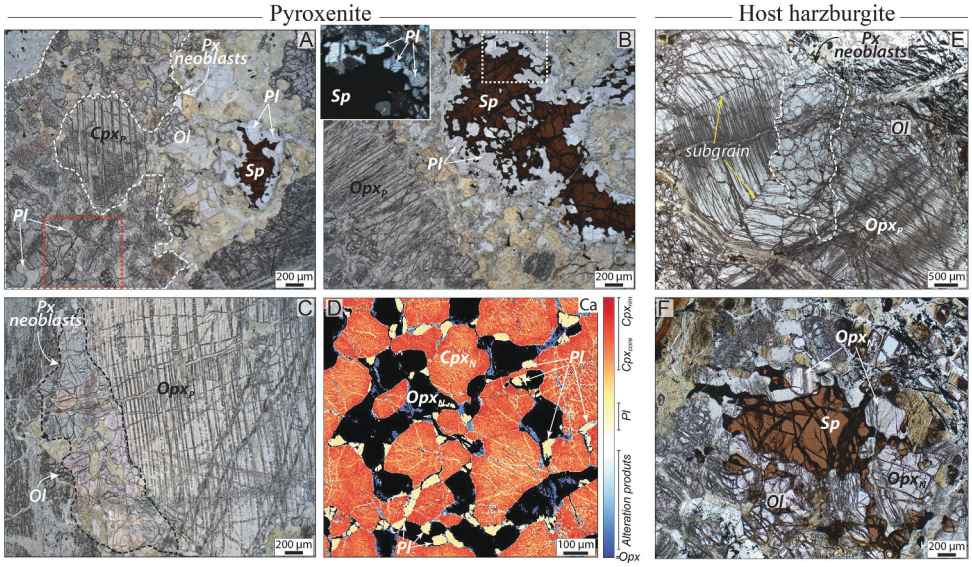

Fig. 3. Microphotographs of the pyroxenite veins (A-D) and their host harzburgites (*E*-F) from the Peyve Seamount in the Doldrums Fracture Zone. A) Neoblastic assemblage grown on an intensely recrystallized and dismembered clinopyroxene porphyroclasts (Cpx_P) in which the mosaic-like uniform texture is composed by newly crystallized clinopyroxene (up to ~200–300 μm), orthopyroxene (~50–100 μm) and plagioclase (~20–50 μm). On the right of the image, an amoeboid spinel is partially replaced by a corona of plagioclase associated with olivine. The red box indicates the location of the chemical map in (D). B) Partially recrystallized orthopyroxene porphyroclasts and typical amoeboid Cr-spinel displaying a corona of fresh plagioclase in a pyroxenite vein. C) Commonly occurring large orthopyroxene porphyroclast (Opx_P) mantled by the clino- and orthopyroxene neoblastic assemblage (Px neoblasts). D) Chemical X-ray map for Ca of the pyroxenes-plagioclase neoblastic assemblage in (A). The colour scale is set to highlight the different mineral phases; note the Ca zonation in the clinopyroxene neoblasts and the well-developed exsolutions lamellae of orthopyroxene. E) Deformed and fractured orthopyroxene porphyroclasts showing subgrain boundaries and partially replaced by a clino- and orthopyroxene neoblastic assemblage; no plagioclase is observed. F) Cr-spinel in the host harzburgite; note that the spinel lacks plagioclase corona. (For interpretation of the references to colour in this figure legend, the reader is referred to the web version of this article.)

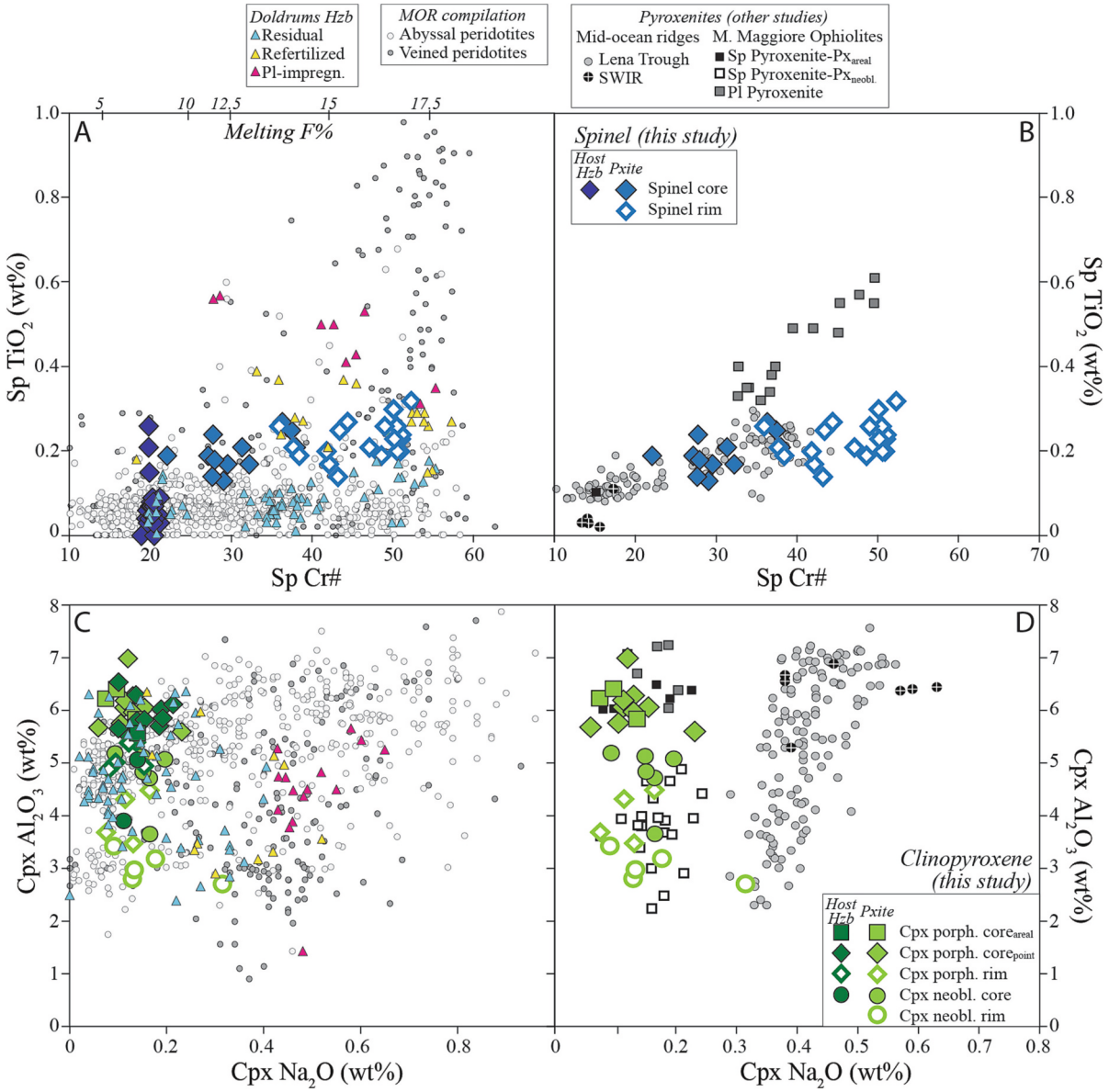

Fig. 4. Spinel (A-B) and clinopyroxene (C—D) major element compositions from the pyroxenite vein (Pxite) and its host harzburgite (Host Hzb). (A-B) Cr# [Cr# = 100 x cationic molar (Cr/(Cr + Al))] values versus TiO_2 contents in spinel; analyses at crystal rims were performed in the pyroxenite only. The degree of mantle melting (F%) in (A) is based on the spinel Cr# following Hellebrand et al. (2002). (C—D) Na_2O versus Al_2O_3 contents in clinopyroxene porphyroclasts and neoblasts. In (A) and (C) we report all data from this study in comparison with *residual*, *refertilized* and *Pl-impregnated peridotites* from the Doldrums FZ (Sani et al., 2020) and abyssal mantle peridotites from mid-ocean ridges (abyssal and veined peridotites from Warren, 2016). In (B) and (D) the compositions of pyroxenites are plotted including those from other spreading centers (Lena Through, Laukert et al., 2014; SWIR, Dantas et al., 2007) and ophiolitic analogues (Monte Maggiore Ophiolite, Corsica, Basch et al., 2019).

core-to-rim Al_2O_3 with increasing Mg#, similar to the clinopyroxene porphyroclasts (Fig. 4d). The plagioclases that mantle spinels and coexisting with the neoblastic assemblage are characterized by high anorthite contents (An = 95.0–97.4; Supplementary Table S1).

The *host harzburgite* of the pyroxenite vein has a porphyroclastic texture and contains large exsolved orthopyroxenes with undulous extinction and kink bands (Fig. 3e), attesting to high-temperature plastic deformation. Olivine is commonly replaced by serpentine (Fig. 3e-f). Irregular grains of brownish spinels have the lowest Cr# (Fig. 4a) and highest Mg# (Supplementary Table S1) among spinels in residual peridotites from the Doldrums FZ. Spinels are locally surrounded by orthopyroxene neoblasts (Fig. 3f). Pyroxene porphyroclasts from the host harzburgite are chemically similar to those in the pyroxenite vein (Fig. 4c). Within the harzburgite, porphyroclasts at the pyroxenite-harzburgite contact and those analyzed away from the contact (~6 cm-distance) display no systematic chemical variations (Supplementary Fig. S1). The low Na_2O and TiO_2 contents in clinopyroxene porphyroclasts from the harzburgite are comparable with the Doldrums residual peridotites, and lower than the Na_2O and TiO_2 contents typical for clinopyroxenes from a global compilation of abyssal peridotites that have reacted with melts (TiO_2 > 0.25%, veined peridotites in Warren, 2016; Fig. 4c and Supplementary Fig. S1). Large orthopyroxene and, more rarely, clinopyroxene porphyroclasts are locally surrounded or replaced by pyroxene neoblasts (Fig. 3e). Contrary to the pyroxenite, the neoblastic assemblage in the host harzburgite does not contain interstitial plagioclase, nor is plagioclase observed surrounding spinel crystals. The neoblasts in the harzburgites are chemically similar to the porphyroclasts in the same rock, attesting to deformation at high temperature conditions (Fig. 4c).

The *Pl-impregnated peridotite* contains large orthopyroxene and minor

clinopyroxene porphyroclasts locally crosscut by microveins mostly containing plagioclase. In sample S09–71/01, plagioclase also occurs as patches associated with euhedral orthopyroxene, indicative of crystallization of silica-saturated melts within the peridotite matrix (see Sani et al., 2020). The textural evidence is confirmed by the high TiO_2 contents in spinel (up to 1.0 wt%) and clinopyroxene crystals (up to 0.5 wt %) at rather low Na_2O concentrations in clinopyroxene.

4.2. Clinopyroxene trace element compositions and Hf—Nd isotope ratios

The trace element compositions of clinopyroxenes in the pyroxenite vein are slightly higher than those of clinopyroxenes from the host harzburgite (e.g., Y; see Supplementary Fig. S1). The trace element contents in pyroxenes from the pyroxenite-harzburgite contact are similar to those in the host harzburgite (i.e., at ~6 cm distance from the contact; Supplementary Fig. S1). Compared to the porphyroclasts, clinopyroxene neoblasts have higher middle REE concentrations and are depleted in Sr compared to similarly incompatible elements (Fig. 5). Given the increase in clinopyroxene-plagioclase partition coefficient ratios of the REE with decreasing temperature (e.g., Witt-Eickschen and O'Neill, 2005; Sun et al., 2017), the REE composition of clinopyroxene neoblasts is consistent with crystallization under plagioclase-facies conditions, which is also supported by the textural relationships (see Fig. 3b and Fig. 3d). In the same line of evidence, because the Sr partition coefficient is higher in plagioclase than in clinopyroxene (see Sun et al., 2017), the Sr depletion in neoblasts compared to the porphyroclasts reflects precipitation of plagioclase in equilibrium with the neoblastic assemblage.

The CI-chondrite normalized (Sun and McDonough, 1989) patterns of clinopyroxene porphyroclast cores display strong light relative to heavy REE depletions (average Ce_N/Yb_N = 0.007), slight middle to heavy REE fractionations (average Sm_N/Yb_N = 0.17) and low Zr and Hf concentrations (on average, Zr = 0.33 ppm and Hf = 0.11 ppm), similar to clinopyroxenes in the residual peridotites from the Doldrums FZ (Sani et al., 2023; Fig. 5a). Despite having a stronger depletion in Zr and weak Eu and Sr depletions relative to similarly incompatible elements, the trace element patterns of the clinopyroxenes from the pyroxenite vein are subparallel to clinopyroxenes from the *Pl-impregnated peridotite* that plot at higher concentration levels (Fig. 5a). The depletions in light REE, Sr, Zr and Hf are greater than those expected for clinopyroxenes in equilibrium with average MORB, but similar to those in clinopyroxenes from other depleted abyssal (Laukert et al., 2014; Dantas et al., 2007) and ophiolitic (e.g., Basch et al., 2019; Fig. 5b) pyroxenites. Notably, the Doldrums pyroxenite is distinct from the pyroxenites sampled at 10°E of the Southwest Indian Ridge (Warren et al., 2009), which contain clinopyroxenes with nearly flat REE patterns (Fig. 5b).

The $^{147}Sm/^{144}Nd$ increase from 0.46 in the *Pl-impregnated peridotite* to 0.52 in the pyroxenite and 0.76 in the host harzburgite (Table 1; Fig. 6), but are coupled to similarly low $^{143}Nd/^{144}Nd$ (i.e., = 0.51297 for the Pl-peridotite, 0.51318 for the pyroxenite vein, and 0.51320 for the host harzburgite) that are typical for Atlantic MORBs (average $^{143}Nd/^{144}Nd \approx 0.51314$; see Fig. 1). There is no correlation between $^{143}Nd/^{144}Nd$ and $^{147}Sm/^{144}Nd$ when all data from the Doldrums FZ are considered (Sani et al., 2023; Fig. 6). On the other hand, the Hf isotope ratio of the pyroxenite vein ($^{176}Hf/^{177}Hf = 0.28391$, $\varepsilon Hf = 40.3$) by far exceeds that of the host harzburgite ($^{176}Hf/^{177}Hf = 0.28323$; Fig. 6) and of erupted MORBs along the Mid-Atlantic Ridge (see Fig. 1). Despite this difference in Hf isotope ratios, the pyroxenite and host harzburgite have comparable $^{176}Lu/^{177}Hf$ of 0.18–0.19 (Fig. 6). Notably, the high Hf-isotope ratio of the clinopyroxene separates from the pyroxenite approaches those of clinopyroxenes from the Doldrums *refertilized peridotites* (Sani et al., 2023; Fig. 6), whereas clinopyroxenes from the host harzburgite have MORB-like Hf isotope ratios comparable to those in clinopyroxenes from the *residual* peridotites from the Doldrums FZ (Fig. 6). The *Pl-impregnated peridotite* also has high $^{176}Hf/^{177}Hf$ (= 0.28359) but low $^{176}Lu/^{177}Hf$ (= 0.09) and MORB-like $^{143}Nd/^{144}Nd$ (Fig. 6), in between the pyroxenite and its host harzburgite.

5. Discussion

5.1. Origin of the pyroxenite vein

5.1.1. Crystallization from an ultra-depleted melt

Pyroxenite veins or layers are a volumetrically minor, but ubiquitous component in the oceanic lithosphere (<5% in the global compilation of abyssal peridotites; Warren, 2016), and in ophiolitic or orogenic mantle exposures (e.g., Garrido and Bodinier, 1999; Python and Ceuleneer, 2003; Downes, 2007; Bodinier et al., 2008; Gysi et al., 2011; Sanfilippo and Tribuzio, 2011; Borghini et al., 2016; Basch et al., 2019). Pyroxenites in subcontinental and orogenic peridotites are related to ancient, recycled crust that has become stretched, boudinaged, and intermingled with the peridotitic mantle (Allégre and Turcotte, 1986). In abyssal

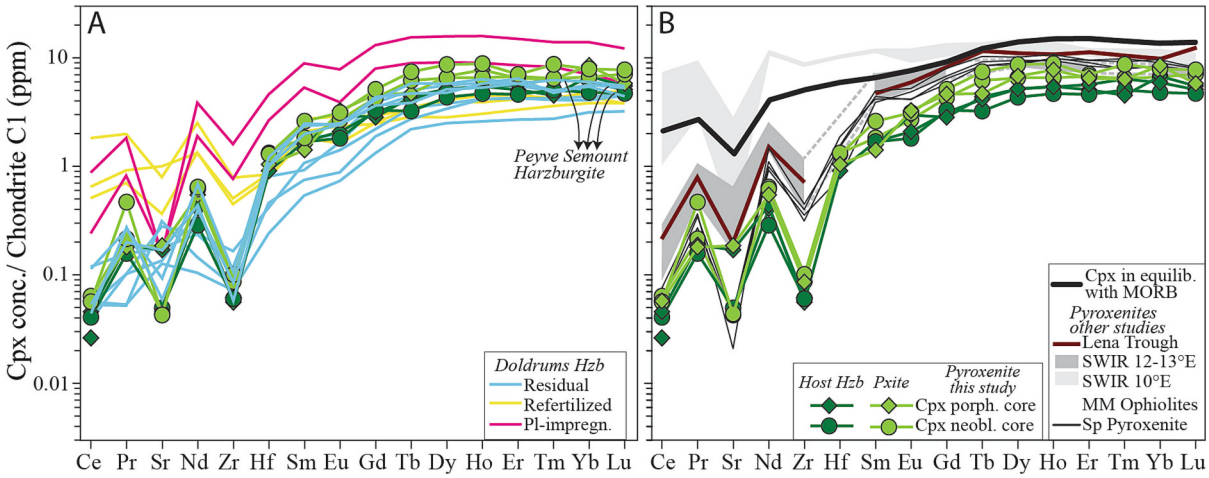

Fig. 5. Chondrite-normalized incompatible trace element concentrations in clinopyroxene porphyroclasts and neoblasts from the Doldrums pyroxenites and their host harzburgite. For comparison we report in (A) the composition of clinopyroxenes in residual, refertilized and Pl-impregnated harzburgites from the Doldrums Fracture Zone (Sani et al., 2020), and in (B) the compositions of clinopyroxenes in pyroxenites from other oceanic spreading centers (Lena Through [average composition], Laukert et al., 2014; 12°-13° E SWIR, Dantas et al., 2007; 10°E SWIR, Warren et al., 2009) and ophiolitic analogues (Monte Maggiore Ophiolite, Corsica, Basch et al., 2019). The average MORB clinopyroxene composition was calculated in equilibrium with the average N-MORB from Gale et al. (2013) using the partition coefficient selection in Ferrando et al. (2018). Normalizing values are after Sun and McDonough (1989).

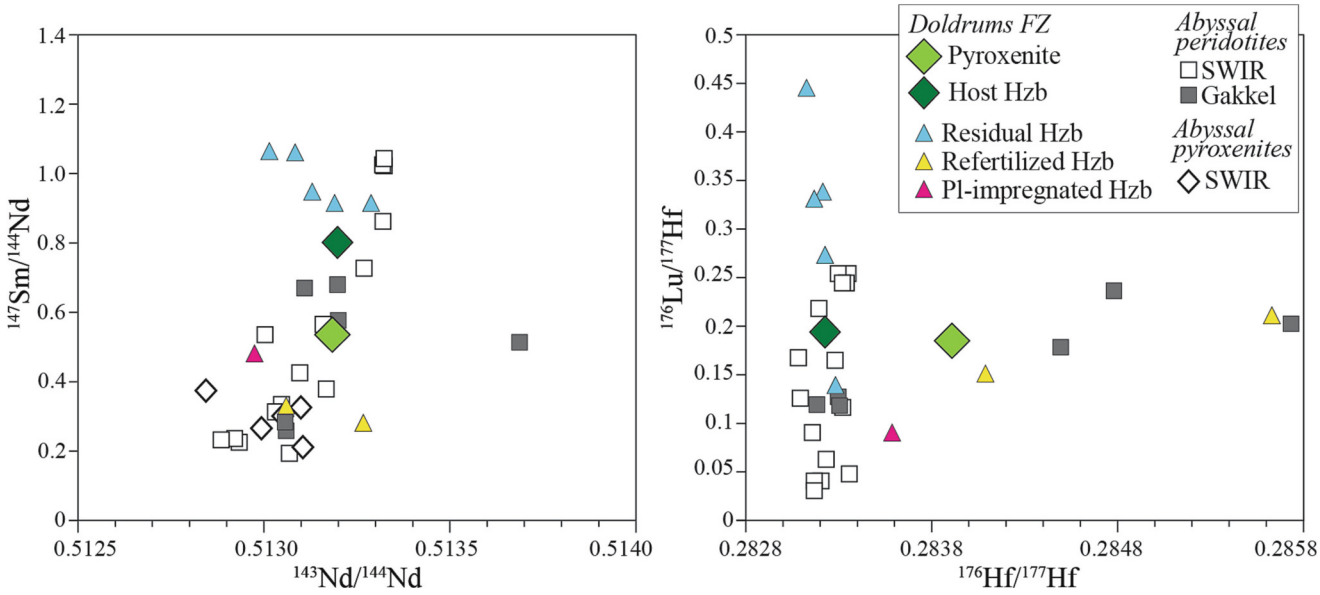

Fig. 6. $^{147}Sm/^{144}Nd$ versus $^{143}Nd/^{144}Nd$ and $^{176}Lu/^{177}Hf$ versus $^{176}Hf/^{177}Hf$ of clinopyroxene in the pyroxenite and host harzburgite. The Nd isotope compositions of clinopyroxenes in abyssal pyroxenites from the SouthWest Indian Ridge are also reported (Warren et al., 2009). For comparison, we also plot the compositions of clinopyroxenes in residual, refertilized and Pl-impregnated harzburgites from the Doldrums Fracture Zone (Sani et al., 2023) and other mid-ocean ridges (SouthWest Indian Ridge, Mallick et al., 2014, 2015; Gakkel Ridge, Stracke et al., 2011).

peridotites, however, pyroxenites mostly occur as veins formed by the recent crystallization of basaltic melts ascending through the sub-ridge mantle (e.g., Juteau et al., 1990; Dantas et al., 2007; Warren et al., 2009).

The abyssal pyroxenite investigated in this study is not boudinaged, thereby suggesting that this vein was not deformed by asthenospheric mantle flow under high temperatures. Rather, the sharp and anastomosing contacts with the host harzburgite (Fig. 2b) are consistent with formation in recent times, at relatively low temperature conditions typical for the oceanic lithosphere. The higher Cr# and TiO_2 of spinel cores in the pyroxenite compared to the host-harzburgite (Fig. 4a) further suggest that spinels from the pyroxenite are crystallized from a melt. Moreover, the highly radiogenic Hf isotope ratios (Fig. 6) coupled to strong light versus heavy REE depletions (Fig. 5) in the clinopyroxenes from the studied pyroxenite contrast to the lower Nd and Hf isotope ratios expected for ancient, recycled oceanic crust (e.g., Allégre and Turcotte, 1986; Chauvel and Blichert-Toft, 2001). The extremely low light REE contents and the strong Zr depletions in clinopyroxenes from the Doldrums pyroxenite (Fig. 5) therefore suggest that they originate by crystallization from an incompatible element depleted, i.e., ultra-depleted melt within the oceanic lithosphere. Hence, in line with previous studies of abyssal pyroxenites (e.g., Dantas et al., 2007; Warren et al., 2009; Laukert et al., 2014), we infer that the Doldrums pyroxenite is of magmatic origin and represents recent magma addition into the mantle beneath the present-day mid-ocean ridge.

However, abyssal pyroxenites may also form by 'reactive melt stagnation', i.e., they could be produced by reaction of migrating melts with the ambient peridotite (e.g., Laukert et al., 2014). Notably, the host peridotites around pyroxenites that formed by reactive melt percolation (e.g., Borghini et al., 2020; Hidas et al., 2021; Kempton et al., 2022) and those generated in high pressure reactive crystallization experiments (Borghini et al., 2022), show large chemical variations at the centimeter to decimeter scale. The host harzburgite of the Doldrums pyroxenite displays no geochemical gradients as pyroxene porphyroclasts are chemically homogeneous at the pyroxene-host harzburgite contact and away from it (Supplementary Fig. S1). Moreover, textural features commonly related to pervasive melt-peridotite interaction, such as interstitial pyroxenes or vermicular olivine (e.g., Seyler et al., 2007; Kaczmarek and Müntener, 2008; Rampone et al., 2008; Sanfilippo and Tribuzio, 2011; Basch et al., 2018; Ferrando et al., 2018; Sanfilippo et al., 2022), are absent in the pyroxenite vein or along the pyroxenite-host peridotite contact. Accordingly, the clinopyroxenes in both the pyroxenite vein and host harzburgite have low TiO_2 (Fig. 4c-d; Supplementary Table S1) and lack enrichments in the most incompatible elements that are a typical indicator for melt-rock reaction processes (Fig. 5). These textural and chemical signatures show that the pyroxenite-forming melt was not modified by reaction with the host harzburgite prior to or during pyroxenite emplacement.

Yet, the similar trace element compositions of the clinopyroxenes in the pyroxenites and those in the host harzburgite (Supplementary Fig. S1) may be the result of equilibration via element diffusion during pyroxenite formation, at both high temperatures and subsolidus conditions. Element diffusion strongly depends on concentration gradients and on the diffusion coefficients. MORB-like melts have much higher light REE than, and similar heavy REE concentrations to the host harzburgite. Hence, if the pyroxenite-forming melt had a MORB-like composition, the strong chemical gradient between melt and the depleted host peridotite should have caused diffusion of light REE from the melt to the host rock. This, therefore, would have led to intermediate concentrations of light REE in the resulting melt, with little effect on the heavy REE concentrations. At the same time, diffusion would have reset the Nd—Hf isotopic composition of the pyroxenite and host harzburgite (Lesher, 1990). Notably, the heavy REE contents of the clinopyroxenes from the investigated pyroxenite are overall similar to those of a residue of a DM-like peridotite and remarkably lower than those of clinopyroxenes in equilibrium with MORBs (average N-MORB from Gale et al. (2013b); Fig. 5b), but their Hf isotopic composition is higher (Fig. 6). The significantly higher $^{176}Hf/^{177}Hf$ of the pyroxenite compared to the host harzburgite, together with the similar REE contents, therefore argues against diffusive re-equilibration during formation of the pyroxenite vein. Nonetheless, it is possible that element diffusion occurred but to minor extents, in that it did not erase the contrast in Hf isotope composition. These observations suggest that the low trace element concentrations (i.e., 'ultra-depleted' character; Fig. 5) of the pyroxenite parental melt are a primary feature that is inherited from its source rock.

We therefore conclude that the studied pyroxenite vein formed by fractional crystallization of an ultra-depleted melt that was derived from a different source than the host harzburgite. The lack of heavy REE

depletion relative to the middle REE in the pyroxenite clinopyroxenes indicates that garnet was not involved during production of the pyroxenite parental melt and, therefore, it mostly formed within the spinel stability field. The occurrence of primary abundant spinel in the pyroxenite imply that crystallization also took place at spinel-facies conditions, thereby suggesting segregation of the pyroxenite-forming melt soon after it was produced.

5.1.2. Source of the pyroxenite-forming melt

Similar to the pyroxenite, the mantle source of the pyroxenite-forming melt must have had high Hf isotope ratios, but MORB-like Nd isotope ratios. This requires that the ultra-depleted peridotite mantle developed with high time-integrated Lu/Hf, thus calling for ancient events of melt extraction (melting model showing Hf—Nd radiogenic growth of a residual peridotite is reported in Fig. 7a). In contrast, Sm/Nd evolved with only moderate time-integrated values. Such decoupled Lu/Hf and Sm/Nd, and with time, Nd—Hf isotopic signatures have been documented in abyssal peridotites from the Gakkel Ridge (Fig. 6 and Fig. 7). They have been explained by reaction of ultra-depleted peridotite with MORB-like melts; the high Hf isotope ratios of the ultra-depleted peridotite are preserved during melt-rock reaction, whereas the Nd isotope ratios are effectively reset to values close to that of the melt (Stracke et al., 2011). The reason is that ultra-depleted peridotites have higher Sm/Nd but lower Nd contents than MORB-like melts. The comparatively small difference in Hf contents between ultra-depleted peridotite and MORB-like melts means that higher extents of melt-rock interaction are required to completely reset the Lu/Hf (and Hf isotope ratios) toward those of the melt than for resetting the Sm/Nd and Nd isotope ratios, resulting in Nd—Hf isotope ratios of reacted peridotites that preserve high Hf, but MORB-like Nd isotope ratios (Bizimis et al., 2003; Stracke et al., 2011).

Peridotites with much higher Hf isotope ratios than MORB, but MORB-like Nd isotope ratios also occur at the Doldrums FZ; these are the *refertilized peridotites* according to the grouping by Sani et al., (Sani et al., 2020, Sani et al., 2023; Fig. 6 and Fig. 7). Sani et al. (2023) showed that the Hf—Nd isotope ratios of the *refertilized peridotites* can be reproduced by ancient melt–rock interactions (500 Ma) of ultra-depleted peridotite that formed by 5% to 10% partial melting between 0.5 Ga and up to 2 Ga ago (Fig. 7a) and partially equilibrated (from 70% to 85% re-equilibration) with a MORB-like melt (average *E*-MORB composition from (Gale et al., 2013b), which was progressively modified by the reaction (Fig. 7b). Independent of the degrees of ancient mantle melting (i.e., 5%, 7% and 10% in Fig. 7a), these melt-rock interaction models numerically demonstrated that peridotites modified by interaction with chemically alike migrating melts follow similar trajectories in Hf—Nd isotopic space. The chance of preserving radiogenic Hf with MORB-like Nd isotope ratios is strongly dependent on the extent of melt-rock interaction (Fig. 7b). Peridotites similar to the *refertilized peridotites*

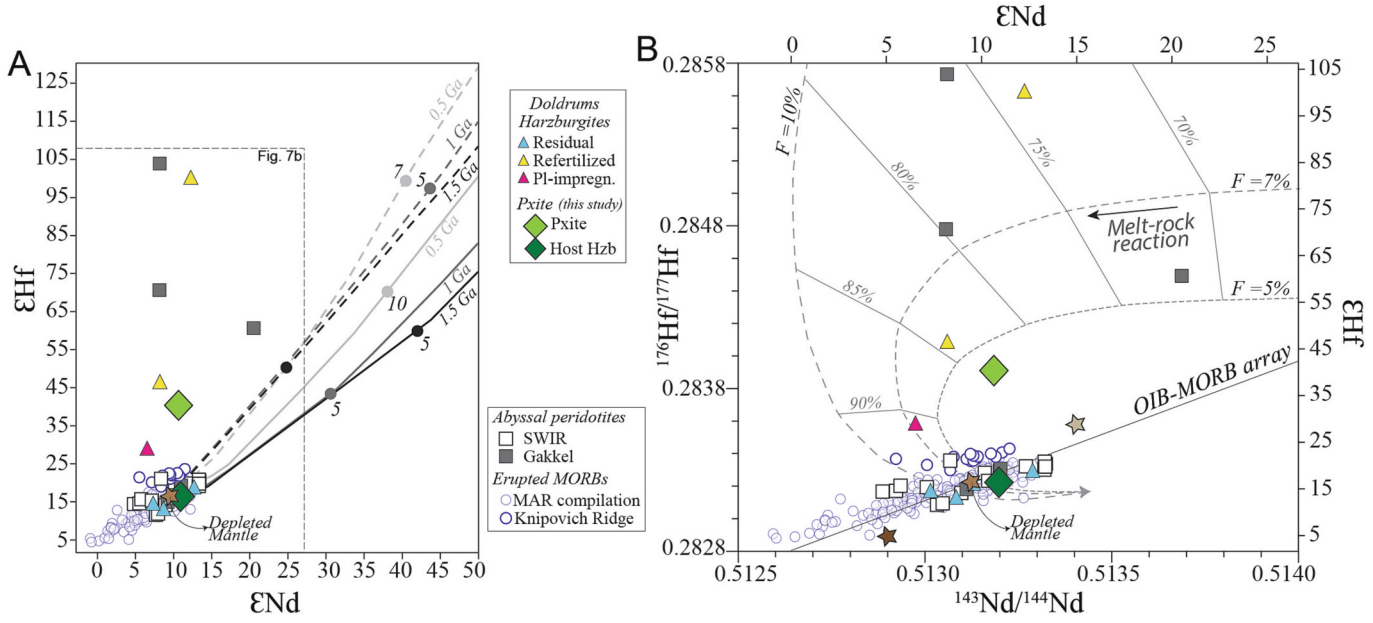

Fig. 7. Diagrams showing the Hf and Nd isotope ratios of clinopyroxenes in the studied pyroxenite and host harzburgite from the Doldrums Fracture Zone. The isotopic compositions of clinopyroxenes in residual, refertilized and Pl-impregnated harzburgites from the Doldrums FZ (Sani et al., 2023) are also reported. For comparison, we plot the isotopic compositions of abyssal peridotites from ultraslow-spreading ridges (SouthWest Indian Ridge, Mallick et al., 2014, 2015; Gakkel Ridge, Stracke et al., 2011) compared to MORBs from the Mid-Atlantic Ridge (compiled from PetDB, www.earthchem.org/petdb) and Knipovich Ridge (Sanfilippo et al., 2021). For reference, estimates of average Depleted Mantle (brown star; Faure, 1986; Griffin et al., 2000; light grey star; Salters and Stracke, 2004) and the low-εHf Depleted Mantle (dark brown star; Salters et al., 2011) are shown. Calculated Hf—Nd isotopic evolution lines are for (A) depleted mantle residues after partial melting at 0.5 (grey), 1 (dark grey), and 1.5 Ga ago (black) starting in the garnet stability field (3.5%) followed by further melting at spinel facies (solid lines), and exclusively in the spinel stability field (dashed lines); (B) depleted mantle residues after 5, 7 and 10% of partial melting and subsequently involved in melt-rock interaction with a MORB-type melt (average E-MORB from Gale et al., 2013). Melting was reproduced using a dynamic melting model (following Stracke et al., 2003) with residual porosity fixed at 1% and percentage of melting per km at 0.15%; the initial source composition is the average depleted mantle (DM) estimate of Salters and Stracke (2004). Garnet melting is assumed to begin at 100 km for a degree of melting F = 0–3.5% followed by further melting in the spinel stability field. Spinel melting starts at 75 km. Melting reactions are recalculated at 60 km, 48 km, 33 km, 24 Km following the phase relations from Longhi (2002). Modelling of melt-rock reactions was performed using the Assimilation-Fractional Crystallization of DePaolo (1981) assuming constant melt mass during reaction and a ratio of mass assimilated to mass crystallized of ~0.99 reproducing a re-enriched peridotite gradually acquiring a lherzolitic composition by preferential dissolution of olivine and crystallization of clinopyroxene. The melt-rock interaction process is modelled at increasing degree of reaction (light grey numbers indicate the degree), which represent the extent to which residual mantle re-equilibrated with the constantly modified melt, from <70% re-equilibration to 99% re-equilibration falling in the field of MORBs compositions (peridotite nearly completely re-equilibrated with melt). Numerical models of partial mantle melting and Assimilation-Fractional Crystallization processes are taken from Sani et al. (2023). Mineral/melt element partition coefficients are from Salters and Stracke (2004). (For interpretation of the references to colour in this figure legend, the reader is referred to the web version of this article.)

from the Doldrums FZ could therefore be the source of the parental melt of the investigated pyroxenite. Melt-rock interactions and addition of a fusible phase produced a mineralogically more fertile mantle, i.e. clinopyroxene-bearing, that by partial melting generated a basaltic melt having element compositions similar to a primary trace element-depleted MORB with a isotopically radiogenic signature. Hence, the ultra-depleted character in term of incompatible elements and Hf isotopes did not impede the crystallization of a clinopyroxene-bearing assemblage as that of the Doldrums pyroxenite.

Given the variability in Hf-isotope ratios in the Doldrums *refertilized peridotites* and the occurrence of peridotites with MORB-like Hf and Nd isotope ratios (i.e., the *residual peridotites* of Sani et al., 2020, 2023), the peridotitic mantle at the Doldrums FZ is highly heterogeneous, recording various extents of melt-rock interactions (see Sani et al., 2023). In detail, the pyroxenite has lower Hf isotope ratios for similar Nd isotope ratios than the *refertilized peridotites* from the Doldrums FZ. We used the same numerical approach as Sani et al. (2023), and thus used the Assimilation-Fractional Crystallization (AFC) model (DePaolo, 1981) to reproduce the isotopic and trace element composition of the mantle source of the pyroxenite-forming melt. We simulated melt-rock interactions involving preferential dissolution of olivine and crystallization of new clinopyroxene. The isotopic composition of the mantle source of the pyroxenite-forming melt was obtained after intermediate to high extents of melt-rock interaction between a refractory peridotite (5% mantle melting ~1 Ga ago) and a MORB-type melt (average E-MORB composition from Gale et al., 2013), when the mantle composition reached up to 80% re-equilibration with the reacting modified melt (Fig. 7b).

5.1.3. *Melting a refractory and refertilized peridotite: Formation of the ultra-depleted melt*

Melts strongly depleted in incompatible elements can be generated as single incremental melt fractions produced by melting a DM-like mantle source (Rampone et al., 1997, 2008; Dijkstra et al., 2003; Suhr et al., 2003; Piccardo et al., 2007; Brunelli and Seyler, 2010; Guarnieri et al., 2012; Basch et al., 2019), or as partly aggregated melts from a more incompatible element depleted peridotite (Stracke et al., 2019; Sanfilippo et al., 2019). Although the light REE-depleted character of the parental melt of the Doldrums pyroxenite may be reproduced by melting of a DM-like source (7–8% melting; Fig. 8), this scenario strongly contrasts with the complex evolution revealed by the isotopic composition involving ancient melting and partial re-equilibration with MORB-type melts.

To evaluate whether an ancient refractory and refertilized mantle source can account for the ultra-depleted trace element composition of the pyroxenite-forming melt, we simulated a process of partial melting (using the dynamic melting model from Stracke et al., 2003) of an anciently refertilized peridotite. The starting trace element compositions of the refertilized mantle peridotites were selected among mantle compositions obtained via the AFC model (DePaolo, 1981) used to reproduce the isotopic composition of clinopyroxenes from the Doldrums pyroxenite (see previous subchapter). The AFC models

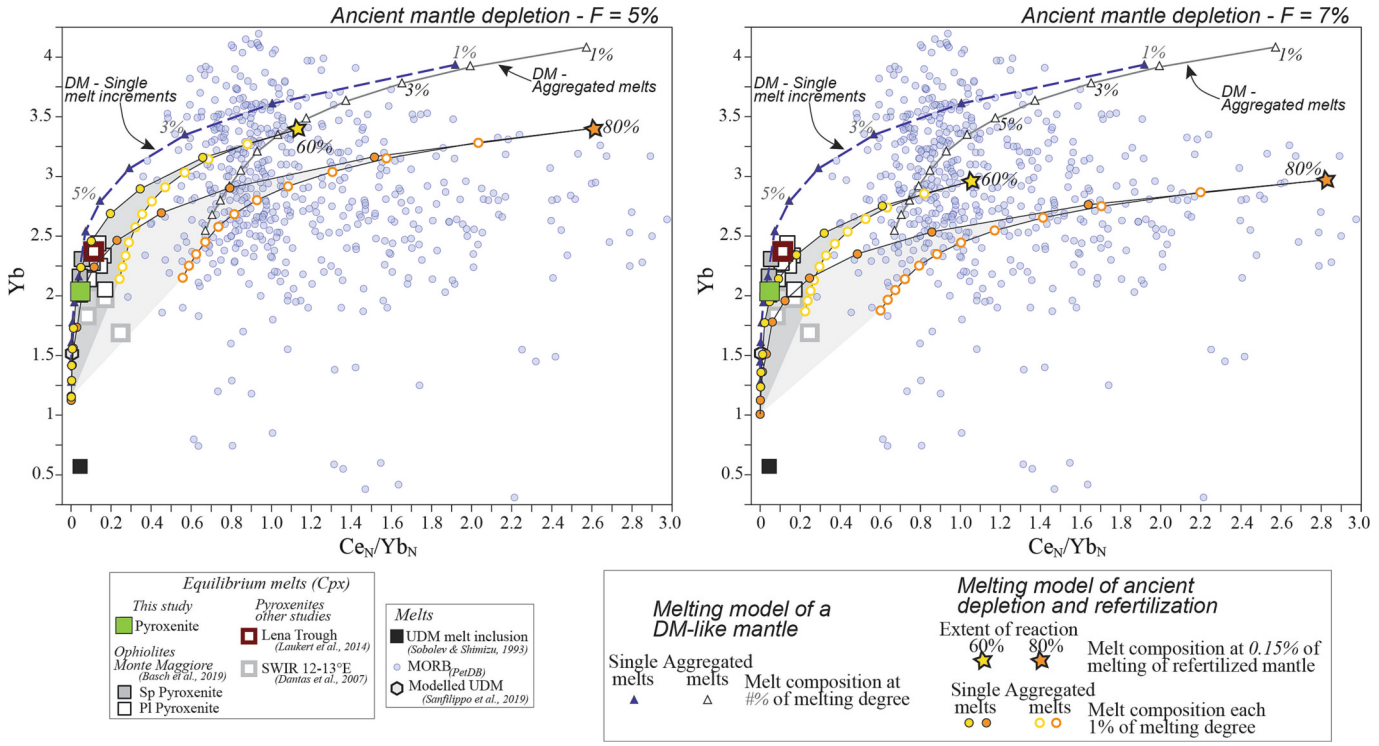

Fig. 8. Diagrams showing Ce_N/Yb_N (N = Chondrite-normalized values) vs Yb compositions of melts calculated in equilibrium with clinopyroxenes in pyroxenite veins from modern mid-ocean ridges (Doldrums FZ, this study; Lena Trough [average composition], Laukert et al., 2014; 12°-13° E SWIR, Dantas et al., 2007) and ophiolitic analogues (Monte Maggiore Ophiolite, Corsica, Basch et al., 2019). For comparison we also show the compositions of MORBs (compiled from PetDB, www.earthchem.org/petdb) and of the ultra-depleted melts documented in an olivine-hosted inclusion (Sobolev and Shimizu, 1993) and modelled by numerical melting models (Sanfilippo et al., 2019). Also shown are the expected Ce_N/Yb_N vs Yb evolution lines for melts produced by partial melting in the spinel stability field of a depleted mantle (DM) source (lines with triangles) and of ancient, residual mantle sources after 5% (A) and 7% (B) ancient melting that were modified by increasing extents of melt-rock reactions (60%: yellow star and dots, 80%: orange star and dots). A dynamic melting model was used assuming melting within the spinel-stability field exclusively and a fixed residual porosity of 1%; partition coefficients are from Salters and Stracke (2004). The DM source is from Workman and Hart, 2005. The starting composition of ancient, purely residual and refertilized mantle is taken from the numerical models performed by Sani et al. (2023); see the text and Fig. 7 for further details. Solid dots and triangles indicate composition of single melts increments, whereas the empty dots and triangles indicate the compositions of aggregated melts. The stars show melts produced after 0.15% melting of the selected ancient, refractory and refertilized mantle sources. (For interpretation of the references to colour in this figure legend, the reader is referred to the web version of this article.)

simulate the trace element composition of mantle peridotite residue during ancient melt-rock interactions (500 m.y. ago) between a MORB-type melt and an ultra-depleted peridotite residual after 5% and 7% melting (~1 Ga ago). The AFC calculations were interrupted at 60% and 80% of re-equilibration to obtain a total of four end-member starting mantle compositions for the melting models. These starting compositions of anciently refertilized mantle peridotites (see Supplementary Table S2) generate aggregated melts that are more enriched in middle-heavy REE and are not as light REE depleted as the Doldrums pyroxenite (Fig. 8).

Notably, the chemistry of pyroxene porphyroclasts testify that the pyroxenite was emplaced >27 km beneath the ridge axis and that the parental melt was produced within the spinel stability field (see section *5.1.1 Crystallization from an ultra-depleted melt*), which is located at <60 km-depth beneath transform systems like the Doldrums FZ (Ligi et al., 2005). Since melt extraction and mixing beneath MORs is most efficient when high porosity channels form at shallower levels (e.g., Liang et al., 2011; Katz and Weatherley, 2012; Liu and Liang, 2019), it is very likely that melts generated within the spinel stability field of the melting region are not fully aggregated at depths of ~30 km. The pyroxenite-forming melt may, therefore, has been extracted from its mantle source and migrated only over short distances, thus preventing high extents of melt aggregation before crystallizing and forming the pyroxenite vein. In this scenario, incremental melt fractions by low extents of mantle melting (4 to 6%) best produce the strong light REE depletion measured in the pyroxenite clinopyroxenes (Fig. 8).

Ultra-depleted melts can thus be produced by low degrees of partial melting of a residual mantle peridotite, which locally preserves a chemical record for ancient melting and is mineralogically fertile as consequence of melt-rock reaction in the past. The isotopic compositions of ultra-depleted mantle domains (i.e., high Hf isotope ratios) are therefore most likely preserved in melts only if these migrated over short time distances after melting, and segregated prior to extensive mixing with other (more trace element-rich) melts migrating through the melt drainage network.

5.2. Crystallization at depth and evolution during exhumation at low pressure

The pyroxenite vein was originally a spinel-bearing websterite that mainly consisted of large clinopyroxene and orthopyroxene crystals, which are now partially preserved as deformed and dismembered porphyroclasts. Experimental studies of MORB crystallization show that early saturation of pyroxenes requires high-pressure (7–10 kbar; e.g., Tormey et al., 1987; Husen et al., 2016). The ortho- and clinopyroxenes formed under these pressure conditions typically have high Al_2O_3 concentrations (> 4.5 wt%; Villiger et al., 2004) and high MgO. Therefore, as suggested for other oceanic pyroxenite layers (Seyler et al., 2001; Dantas et al., 2007; Laukert et al., 2014; Basch et al., 2019), the high Al_2O_3 content (~ 6–7 wt%; Fig. 4d; Supplementary Table S1) and high Mg# of the cores of the pyroxene porphyroclasts indicate melt segregation and pyroxenite emplacement occurred at >27 km depth ($P > 9$ kbar) within the spinel stability field. We used areal analyses of cores of porphyroclastic clinopyroxene and adjacent orthopyroxene couples to determine the temperature of melt emplacement (as proxy for the pyroxene composition prior to exsolution upon cooling). Equilibrium temperatures calculated with the two-pyroxene Fe—Mg geothermometer (Taylor, 1998) range from 1140– to 1250 °C (Supplementary Table S3), further supporting pyroxenite formation at spinel-facies conditions.

In the pyroxenite vein, the large porphyroclasts are now partially replaced by a well-equilibrated neoblastic assemblage of clinopyroxene, orthopyroxene and plagioclase (Fig. 3a and Fig. 3c-d), which is in textural equilibrium (Fig. 3d). The occurrence of interstitial plagioclase is commonly attributed to melt impregnation involving diffuse migration, entrapment, and crystallization of melts within the shallow lithospheric mantle (e.g., Dick, 1989; Rampone et al., 1997, 2008; Tartarotti et al., 2002; Cannat et al., 2006; Piccardo et al., 2007; Tamura et al., 2008; Basch et al., 2018; Whattam et al., 2022). Alternatively, interstitial plagioclase may form by metamorphic recrystallization of Ca-rich plagioclase + olivine, at plagioclase-facies conditions (e.g., Hamlyn and Bonatti, 1980; Hoogerduijn Strating et al., 1993; Rampone et al., 1993; Cannat and Seyler, 1995; Canil et al., 2003; Montanini et al., 2006; Borghini et al., 2011). The low TiO_2 contents of spinels in the studied pyroxenite differ from the characteristic association of high-Ti spinel and interstitial orthopyroxenes that is commonly observed in melt-impregnated peridotite (e.g., Dick, 1989; Rampone et al., 1997; Tartarotti et al., 2002; Tamura et al., 2008; Basch et al., 2018). Also, the lack of plagioclase in the host harzburgite (Fig. 3f) makes it unlikely that a melt percolated only through the 2 mm-thick pyroxenite without affecting the host harzburgite. Even so, it might be plausible that melt percolation occurred earlier in the pyroxenite vein precipitating plagioclase and then infiltrated into the host harzburgite where the ultra-depleted composition of the melt (low Al and Ca) hampered plagioclase crystallization. However, the pyroxenite-to-harzburgite (away from the contact) mineral compositions show no chemical gradients (Supplementary Fig. S1), which is in contradiction with a process of melt percolation from the pyroxenite into the harzburgite. Rather, the occurrence of plagioclase + olivine coronas around all amoeboid spinel crystals in the studied pyroxenite (Fig. 3a-b) resemble metamorphic textures typically observed in lithospheric mantle that re-equilibrated under plagioclase-facies conditions (e.g., Hamlyn and Bonatti, 1980; Hoogerduijn Strating et al., 1993; Rampone et al., 1993; Cannat and Seyler, 1995; Borghini et al., 2011). Moreover, the core-to-rim decreasing Al_2O_3 contents in the analyzed pyroxene porphyroclasts (Fig. 4d) and the significant core-to-rim increase of Cr# in spinel crystals (Fig. 4d) are consistent with the mineralogical evolution documented by subsolidus experiments (i.e., performed at decreasing pressure) on lherzolitic compositions (e.g., Borghini et al., 2011). We conclude that the composition of the Doldrums pyroxenite, with relatively Al and Ca-rich pyroxene porphyroclast cores, enhanced the subsolidus recrystallization (i.e., metamorphic) under plagioclase-facies conditions (Borghini et al., 2016; Borghini and Fumagalli, 2018), whereas the refractory composition prevented plagioclase recrystallization in the host harzburgite.

In the pyroxenite, the sub-solidus re-equilibration at low temperature also led to the formation of clinopyroxene neoblasts with high middle to heavy REE (Fig. 5), caused by the temperature-dependent decrease in pyroxene-plagioclase trace element partition coefficients (e.g., Sun et al., 2017). Using the two-pyroxenes Fe—Mg geothermometer (Taylor, 1998) coupled with the Forsterite–Anorthite–Ca-Tschermak–Enstatite (FACE) geobarometer (Fumagalli et al., 2017) we investigated the plagioclase-facies thermo-barometric evolution of the pyroxenites. Strontium depletions relative to neighboring elements in the cores of neoblastic clinopyroxenes (Fig. 5) show that plagioclase crystallized together with nucleating neoblasts. Because the cores of neoblastic pyroxenes are commonly exsolved (Fig. 3c), we used areal analyses of selected couples of crystal cores of neoblastic pyroxenes and adjacent plagioclase. This approach allows estimating the P-T conditions for crystallizing the early plagioclase-facies assemblage at ~1040–1060 °C (two-pyroxenes Fe—Mg geothermometer; Taylor, 1998; Supplementary Table S3) and 5.7 ± 0.2 kbar (Supplementary Table S4). These estimates place the spinel to plagioclase transition at ~17 km depth (pressure gradient = 1 kbar / 3 km-depth), i.e., within the mantle lithosphere beneath the Doldrums FZ.

Finally, the development of exsolution lamellae in the pyroxene neoblasts within the pyroxenite vein indicates further cooling after crystallization of the plagioclase-bearing neoblastic assemblage. Equilibrium temperature estimates on rims of pyroxene neoblasts (T at rim = 850–920 °C) are lower than those calculated for the crystal cores (Supplementary Table S3). The progressive decrease in temperature likely drove Ca diffusion into neoblastic clinopyroxene leading to the

observed core-to-rim increase in CaO contents (Fig. 3d).

To summarize, the pyroxenite-forming melt segregated at deep levels within the oceanic lithosphere. Melt segregation occurred within a mantle harzburgite (i.e., host harzburgite), of which the strong depletion in light relative to heavy REE (Fig. 5a) denote melting prior to pyroxenite emplacement. Notably, before recent processing beneath the spreading center, the host harzburgite likely experienced melt-rock interaction processes and advanced refertilization, evidenced by its MORB-like isotopic composition (Sani et al., 2023). After melt segregation and crystallization of the pyroxenite vein, the pyroxenite-host harzburgite association was exhumed to shallower lithospheric levels; the variation in pressure-temperature conditions drove precipitation of metamorphic plagioclase within the pyroxenite. Textures and mineral chemistry indicate that the pyroxenite-host harzburgite association did not undergo melt percolation and melt-rock interactions after pyroxenite emplacement.

5.3. Migration of ultra-depleted melts

The composition of the pyroxenite vein from the Doldrums FZ suggests that ultra-depleted melts migrate through the local lithospheric mantle but get stuck at depth and crystallize not far from where they have been formed. But migration of ultra-depleted melts over greater distances also occurs, as suggested by the plagioclase-pyroxene pockets and veins within the *Pl-impregnated peridotites* from the Doldrums FZ (Sani et al., 2020). In detail, using a reactive porous flow numerical model (i.e., the non-dimensional "Plate Model" by Vernières et al., 1997), Sani et al. (2020) previously showed that the high heavy REE concentration in the *Pl-impregnated peridotites* requires intergranular migration of a melt that reacts with the host rock at high melt-rock ratios and high porosity prior to crystallization and closure of the magmatic system. Given the high degrees of melt-rock reaction required to explain the high middle to heavy REE contents in clinopyroxenes from these rocks (see Sani et al., 2020), the low light REE contents indicate that the percolating melts must have been highly depleted in incompatible elements compared to typical MORBs (i.e., be 'ultra-depleted').

Similar to the pyroxenite, the *Pl-impregnated peridotite* also has Hf isotope ratios higher than those of typical MORB, while having MORB-like Nd isotope ratios (Fig. 6). Because the *Pl-impregnated peridotite* formed by peridotite-melt reaction (see discussion above), these isotopic signatures can, in this case, be inherited from the pre-existing (i.e., unreacted) peridotite, or derive from the migrating melt. Since the composition of clinopyroxenes in the Doldrums *Pl-impregnated peridotites* was completely modified by the reaction and re-equilibrated with the reacting melt (Sani et al., 2020), its isotopic ratios must have been inherited from the migrating melt. Thereby, such melt ultra-depleted in incompatible elements was also produced by melting of a refractory and refertilized mantle source. The observed occurrence of melts originated from ultra-depleted and refertilized peridotites, either crystallized in pyroxenite veins or interstitially between the peridotitic crystal-matrix, suggests that such refractory domains can contribute to sub-ridge melt production until all clinopyroxene is consumed.

6. Summary and conclusions

In this study we document migration, segregation and crystallization of ultra-depleted melts in the sub-ridge mantle exposed at the Doldrums FZ in the Equatorial Mid Atlantic Ridge. Such ultra-depleted melts either segregated into discrete layers to form the studied pyroxenite or substantially modified the pre-existing mantle matrix generating the *Pl-impregnated peridotites* from the Doldrums FZ. These melts were produced by partial melting of ancient ultra-depleted peridotites that reacted with migrating melts in the past (Fig. 8). Given that melt-rock reaction leads to the crystallization of fusible phases (i.e., clinopyroxene), re-crystallization of clinopyroxene likely plays a major role in enhancing subsequent melting of such 'refertilized' ultra-depleted peridotites.

The melt forming the Doldrums pyroxenite was segregated in a cm-scale vein without evidence for interaction with the host rock. The chemistry of pyroxene porphyroclasts (Al contents) testify that the pyroxenite was emplaced at depth > 27 km beneath the ridge axis (see section *5.2*) and that the parental melt was produced within the spinel stability field (see section *5.1*). Notably, the high Na_8 of basalts from the central region of the Doldrums FZ (Sani et al., 2022) indicate low melting extents of a 'cold' underlying mantle, thereby suggesting that the spinel stability extends to depths <60 km-depth beneath the Doldrums FZ, as estimated for similar transform systems (e.g., Romanche FZ, Ligi et al., 2005). Since melt extraction and mixing beneath Mid-Ocean Ridges is most efficient when high porosity channels form at shallower levels (e.g., Liang et al., 2011; Katz and Weatherley, 2012; Liu and Liang, 2019), it is very likely that melts generated within the spinel stability field of the melting region are not fully aggregated at depths of ~30 km, which is supported by the observation that incremental melt fractions by low extents of mantle melting (4 to 6%) best produce the strong light REE depletion measured in the pyroxenite clinopyroxenes (Fig. 8). Although data from this study do not allow to quantify the melt travel distance from its mantle source to segregation depth, it is plausible that the pyroxenite-forming melt migrated only over short distances after extraction. This prevented extensive mixing with other, chemically distinct melts, especially those from potential incompatible element enriched source components, before crystallizing as pyroxenite vein. The preservation of ultra-depleted melts as discrete pyroxenite layer also shows that renewed melting of ultra-depleted peridotites with a complex history of prior melting and melt-rock reaction can occur, and that such melts migrate through the sub-ridge mantle, which implies that they may contribute to mid ocean ridge magmatism, although to a still unknown extent.

Pyroxenites, together with mineral-hosted melt inclusions, are therefore prime targets for evaluating the significance of ancient ultra-depleted domains in the Earth's mantle, as they are common features in the modern sub-ridge mantle and many massifs of fossil oceanic lithosphere. Oceanic mantle pyroxenites world-wide share similar light REE-depleted composition as ultra-depleted melts recognized at the Doldrums FZ, falling within the REE field comprised between unaggregated and aggregated melts produced by partial melting of an anciently refractory and refertilized mantle source (Fig. 8). Nd isotopes were only measured for five pyroxenites from the Southwest Indian Ridge, whereas no Hf isotopic compositions are available for the other world-wide abyssal pyroxenites. We do not discard the idea that enriched components are also widespread in the abyssal mantle and may be the mantle source of melts forming the oceanic pyroxenites, but this study shows that refractory and refertilized mantle domains can also contribute to generation of melts percolating throughout the lithosphere. Our results call for the need of isotopic measurements of those pyroxenites to decipher whether the nature of their parental melts is derived from mantle sources that experienced a time-integrated history of ancient depletion and refertilization. A comprehensive isotopic dataset of abyssal pyroxenites would substantially improve our understanding of geochemical mantle heterogeneity, allowing for better constraining the proportion of refractory domains within the MORBs source.

CRediT authorship contribution statement

C. Ferrando: Conceptualization, Data curation, Funding acquisition, Investigation, Validation, Visualization, Writing – original draft, Writing – review & editing. **G. Borghini:** Data curation, Methodology. **C. Sani:** Methodology. **F. Genske:** Methodology. **M. Ligi:** Funding acquisition, Investigation. **A. Stracke:** Conceptualization, Investigation, Writing – review & editing. **A. Sanfilippo:** Conceptualization, Funding acquisition, Project administration, Writing – original draft, Writing – review & editing.

Declaration of Competing Interest

The authors declare that they have no known competing financial interests or personal relationships that could have appeared to influence the work reported in this paper.

Data availability

Data will be made available on request.

Acknowledgments

The authors thank Pamela Kempton, Jessica Warren and one anonymous reviewer for the detailed comments on previous version of these manuscript, which led to significant clarifications. We would like to thank the captain, the officers, the crew and the chief scientist Sergey G. Skolotnev of R/V Akademik Nikolaj Strakhov 45. The authors acknowledge Valentin Basch for helpful discussions on a preliminary draft. This study was supported by the Italian Programma di Rilevante Interesse Nazionale (PRIN_2017KY5ZX8) and (PRIN_2022PC9NME) to Alessio Sanfilippo and by the Ministry of University and Research (MUR) through the grant 'ECORD-IODP Italia 2018' attributed to Carlotta Ferrando.

Appendix A. Supplementary data

Supplementary data to this article can be found online at https://doi.org/10.1016/j.chemgeo.2023.121840.

References

Allégre, C.J., Turcotte, D.L., 1986. Implications of a two-component marble-cake mantle. Nature 323, 123–127. https://doi.org/10.1038/323123a0.

Basch, V., Rampone, E., Crispini, L., Ferrando, C., Ildefonse, B., Godard, M., 2018. From mantle peridotites to hybrid troctolites: textural and chemical evolution during melt-rock interaction history (Mt.Maggiore, Corsica, France). Lithos 323, 4–23. https://doi.org/10.1016/j.lithos.2018.02.025.

Basch, V., Rampone, E., Borghini, G., Ferrando, C., Zanetti, A., 2019. Origin of pyroxenites in the oceanic mantle and their implications on the reactive percolation of depleted melts. Contrib. Min. and Petrol. 174, 97. https://doi.org/10.1007/s00410-019-1640-0.

Bizimis, M., Sen, G., Salters, V.J.M., 2003. Hf–Nd isotope decoupling in the oceanic lithosphere. Constraints from spinel peridotites from Oahu, Hawaii. Earth Planet. Sci. Lett. 217 (1–2), 43–58. https://doi.org/10.1016/S0012-821X(03)00598-3.

Bizimis, M., Sen, G., Salters, V.J.M., Keshav, S., 2005. Hf–Nd–Sr isotope systematics of garnet pyroxenites from Salt Lake Crater, Oahu, Hawaii: evidence for a depleted component in Hawaiian volcanism. Geochim. Cosmochim. Acta 69, 2629–2646. https://doi.org/10.1016/j.gca.2005.01.005.

Blichert-Toft, J., Albarède, F., Kornprobst, J., 1999. Lu-Hf isotope systematics of garnet pyroxenites from Beni Bousera, Morocco: implications for basalt origin. Science 283, 1303–1306. https://doi.org/10.1126/science.283.5406.1303.

Bodinier, J.-L., Garrido, C.J., Chanefo, I., Bruguier, O., Gervilla, F., 2008. Origin of pyroxenite–peridotite veined mantle by refertilization reactions: evidence from the Ronda peridotite (Southern Spain). J. Petrol. 49, 999–1025. https://doi.org/10.1093/petrology/egn014.

Borghini, G., Fumagalli, P., 2018. Subsolidus phase relations in a mantle pyroxenite: an experimental study from 0.7 to 1.5 GPa. Eur. J. Mineral. 30 (2), 333–348. https://doi.org/10.1127/ejm/2018/0030-2735.

Borghini, G., Fumagalli, P., Rampone, E., 2011. The geobarometric significance of plagioclase in mantle peridotites: a link between nature and experiments. Lithos 126, 42–53. https://doi.org/10.1016/j.lithos.2011.05.012.

Borghini, G., Rampone, E., Zanetti, A., Class, C., Cipriani, A., Hofmann, A.W., Goldstein, S.L., 2016. Pyroxenite layers in the Northern Apennines' Upper Mantle (Italy) - generation by pyroxenite melting and melt infiltration. J. Petrol. 57, 625–653. https://doi.org/10.1093/petrology/egv074.

Borghini, G., Rampone, E., Zanetti, A., Class, C., Fumagalli, P., Godard, M., 2020. Ligurian pyroxenite-peridotite sequences (Italy) and the role of melt-rock reaction in creating enriched-MORB mantle source. Chem. Geol. 532, 119252 https://doi.org/10.1016/j.chemgeo.2019.07.027.

Borghini, G., Rampone, E., Class, C., Goldstein, S., Cai, Y., Cipriani, A., Hofmann, A.W., Bolge, L., 2021. Enriched Hf–Nd isotopic signature of veined pyroxenite-infiltrated peridotite as a possible source for E-MORB. Chem. Geol. 586, 120591 https://doi.org/10.1016/j.chemgeo.2021.120591.

Borghini, G., Fumagalli, P., Rampone, E., 2022. Melt–rock interactions in a veined mantle: pyroxenite–peridotite reaction experiments at 2 GPa. Eur. J. Mineral. 34, 109–129. https://doi.org/10.5194/ejm-34-109-2022.

Brunelli, D., Seyler, M., 2010. Asthenospheric percolation of alkaline melts beneath the St. Paul region (Central Atlantic Ocean). Earth Planet. Sci. Lett. 289, 393–405. https://doi.org/10.1016/j.epsl.2009.11.028.

Byerly, B.L., Lassiter, J.C., 2014. Isotopically ultradepleted domains in the convecting upper mantle: Implications for MORB petrogenesis. Geology 42, 203–206. https://doi.org/10.1130/G34757.1.

Canil, D., Johnston, S.T., Evers, K., Shellnutt, J.G., Creaser, A., 2003. Mantle exhumation in an early Palaeozoic passive margin, northern Cordillera. Yukon. J. Geology 111, 313–327. https://doi.org/10.1086/373971.

Cannat, M., Seyler, M., 1995. Transform tectonics, metamorphic plagioclase and amphibolitization in ultramafic rocks of the Vema transform fault (Atlantic Ocean). Earth Planet. Sci. Lett. 133, 283–298. https://doi.org/10.1016/0012-821X(95)00078-Q.

Cannat, M., Sauter, D., Mendel, V., 2006. Modes of seafloor generation at a melt-poor ultraslow-spreading ridge. Geology 34, 605–608. https://doi.org/10.1130/G22486.1.

Chauvel, C., Blichert-Toft, J., 2001. A hafnium isotope and trace element perspective on melting of the depleted mantle. Earth Planet. Sci. Lett. 190, 137–151. https://doi.org/10.1016/S0012-821X(01)00379-X.

Cipriani, A., Brueckner, H.K., Bonatti, E., Brunelli, D., 2004. Oceanic crust generated by elusive parents: Sr and Nd isotopes in basalt-peridotite pairs from the Mid-Atlantic Ridge. Geology 32, 657–660. https://doi.org/10.1130/G20560.1.

Dantas, C., Ceuleneer, G., Gregoire, M., Python, M., Freydier, R., Warren, J., Dick, H.J.B., 2007. Pyroxenites from the Southwest Indian Ridge, 9°–16°E: cumulates from incremental melt fraction produced at the top of a cold melting regime. J. Petrol. 48, 647–660. https://doi.org/10.1093/petrology/egl076.

DePaolo, D.J., 1981. Trace element and isotopic effects of combined wall-rock assimilation and fractional crystallization. Earth Planet. Sci. Lett. 53, 189–202.

Dick, H.J.B., 1989. Abyssal peridotite, very slow spreading ridges and oceanic ridge magmatism. In: Saunders, A.D., Norris, M.J. (Eds.), Magmatism in the Ocean Basins, 42. Geol. Soc., London, Special Publ., pp. 71–105

Dijkstra, A.H., Barth, M.G., Drury, M.R., Mason, P.R.D., Vissers, R.L.M., 2003. Diffuse porous melt flow and melt-rock reaction in the mantle lithosphere at a slow-spreading ridge: a structural petrology and LA-ICP-MS study of the Othris peridotite massif (Greece). Geochem. Geophys. Geosyst. 4, 8613. https://doi.org/10.1029/2001GC000278.

Downes, H., 2007. Origin and significance of spinel and garnet pyroxenites in the shallow lithospheric mantle: Ultramafic massifs in orogenic belts in Western Europe and NW Africa. Lithos 99, 1–24. https://doi.org/10.1016/j.lithos.2007.05.006.

Faure, G., 1986. Principles of Isotope Geology. John Wiley and Sons, New York.

Ferrando, C., Godard, M., Ildefonse, B., Rampone, E., 2018. Melt transport and mantle assimilation at Atlantis Massif (IODP Site U1309): constraints from geochemical modeling. Lithos 323, 24–43. https://doi.org/10.1016/j.lithos.2018.01.012.

Frisby, C., Bizimis, M., Mallick, S., 2016. Hf–Nd isotope decoupling in bulk abyssal peridotites due to serpentinization. Chem. Geol. 440, 60–72. https://doi.org/10.1016/j.chemgeo.2016.07.006.

Fumagalli, P., Borghini, G., Rampone, E., Poli, S., 2017. Experimental calibration of Forsterite-Anorthite-Ca-Tschermak-Enstatite (FACE) geobarometer for mantle peridotites. Contrib. Miner. Petrol. 172, 38. https://doi.org/10.1007/s00410-017-1352-2.

Gale, A., Dalton, C.A., Langmuir, C.H., Su, Y., Schilling, J.-G., 2013b. The mean composition of ocean ridge basalts. Geochem. Geophys. Geosyst. 14, 489–518. https://doi.org/10.1029/2012GC004334.

Garrido, C.J., Bodinier, J.-L., 1999. Diversity of mafic rocks in the Ronda peridotite: evidence for pervasive melt-rock reaction during heating of subcontinental lithosphere by upwelling asthenosphere. J. Petrol. 40, 729–754. https://doi.org/10.1093/petroj/40.5.729.

Griffin, W.L., Pearson, N.J., Belousova, E., Jackson, S.E., van Achterbergh, E., O'Reilly, S.Y., Shee, S.R., 2000. The Hf isotope composition of cratonic mantle: LAM-MC-ICPMS analysis of zircon megacrysts in kimberlites. Geochim. Cosmochim. Acta 64, 133–147.

Griffin, W.L., Powell, W.J., Pearson, N.J., O'Reilly, S.Y., 2008. GLITTER: Data reduction software for laser ablation ICP–MS. In: Sylvester, P. (Ed.), Laser Ablation–ICP–MS in the Earth Sciences: Current Practices and Outstanding Issues. Short Course Series. Mineralogical Association of Canada, pp. 307–311.

Guarnieri, L., Nakamura, E., Piccardo, G.B., Sakaguchi, C., Shimizu, N., Vannucci, R., Zanetti, A., 2012. Petrology, trace element and Sr, Nd, Hf isotope geochemistry of the North Lanzo peridotite massif (Western Alps, Italy). J. Petrol. 53, 2259–2306. https://doi.org/10.1093/petrology/egs049.

Guo, P., Niu, Y., Chen, S., Duan, M., Sun, P., Chen, Y., Gong, H., Wang, X., 2023. Low-degree melt metasomatic origin of heavy Fe isotope enrichment in the MORB mantle. Earth Planet. Sci. Lett. 601, 117892 https://doi.org/10.1016/j.epsl.2022.117892.

Gysi, A.P., Jagoutz, O., Schmidt, M.W., Targuisti, K., 2011. Petrogenesis of pyroxenites and melt infiltrations in the ultramafic complex of Beni Bousera, Northern Morocco. J. Petrol. 52, 1676–1735. https://doi.org/10.1093/petrology/egr026.

Hamlyn, P.R., Bonatti, E., 1980. Petrology of mantle-derived ultramafic from the Owen fracture zone, Northwest Indian Ocean: implications for the nature of the oceanic upper mantle. Earth Planet. Sci. Lett. 48, 65–79.

Hellebrand, E., Snow, J.E., Hoppe, P., Hoffmann, A.W., 2002. Garnet-field melting and late-stage refertilization in 'residual' abyssal peridotites from the Central Indian Ridge. J. Petrol. 43, 2305–2338.

Hidas, K., Borghini, G., Tommasi, A., Zanetti, A., Rampone, E., 2021. Interplay between melt infiltration and deformation in the deep lithospheric mantle (External Liguride ophiolite, North Italy). Lithos 380–381 (105855), 2021. https://doi.org/10.1016/j.lithos.2020.105855.

Hoogerduijn Strating, E.H., Rampone, E., Piccardo, G.B., Drury, M.R., Vissers, R.L.M., 1993. Subsolidus emplacement of mantle peridotites during incipient oceanic rifting and opening of the Mesozoic Tethys (Voltri Massif, NW Italy). J. Petrol. 34, 901–927. https://doi.org/10.1093/petrology/34.5.901.

Husen, A., Renat, R.A., Holtz, F., 2016. The effect of H_2O and pressure on multiple saturation and liquid lines of descent in basalt from the Shatsky rise. J. Petrol. 57, 309–344. https://doi.org/10.1093/petrology/egw008.

Jochum, K.P., Nohl, U., Herwig, K., Lammel, E., Stoll, B., Hofmann, A.W., 2007. GeoReM: a New Geochemical Database for Reference Materials and Isotopic Standards. Geostand. Geoanal. Res. 29, 333–338. https://doi.org/10.1111/j.1751-908X.2005.tb00904.x.

Jochum, K.P., Weis, U., Stoll, B., Kuzmin, D., Yang, Q., Raczek, I., Jacob, D.E., Stracke, A., Birbaum, K., Frick, D.A., Günther, D., Enzweiler, J., 2011. Determination of Reference Values for NIST SRM 610–617 Glasses following ISO guidelines. Geostand. Geoanal. Res. 35, 397–429. https://doi.org/10.1111/j.1751-908X.2011.00120.x.

Juteau, T., Berger, E., Cannat, M., 1990. Serpentinized, residual mantle peridotites from the M.A.R. Median valley, ODP Hole 670A (21°10'N, 45°02'W, Leg 109): primary mineralogy and geothermometry. Proc. Ocean Drill. Program Sci. Results 106 (109), 27–45.

Kaczmarek, M.A., Müntener, O., 2008. Juxtaposition of melt impregnation and high-temperature shear zones in the upper mantle; field and petrological constraints from the Lanzo Peridotite (northern Italy). J. Petrol. 49, 2187–2220. https://doi.org/10.1093/petrology/egn065.

Katz, R.F., Weatherley, S.M., 2012. Consequences of mantle heterogeneity for melt extraction at mid-ocean ridges. Earth Planet. Sci. Lett. 335–336, 226–237. https://doi.org/10.1016/j.epsl.2012.04.042.

Kempton, P.D., Stephens, C.J., 1997. Petrology and geochemistry of nodular websterite inclusions in harzburgite, Hole 920D. Proc. Ocean Drill. Program Sci. Results 153, 321–331. https://doi.org/10.2973/odp.proc.sr.153.022.1997.

Kempton, P.D., Mathur, R., Harmon, R.S., Bell, A., Hoefs, J., Shaulis, B., 2022. Cu-isotope evidence for subduction modification of lithospheric mantle. Geochem. Geophys. Geosyst. 23 https://doi.org/10.1029/2022GC010436 e2022GC010436.

Laukert, G., Von der Handt, A., Hellebrand, E., Snow, J., Hoppe, P., Klugel, A., 2014. High-pressure reactive melt stagnation recorded in abyssal pyroxenites from the ultraslow-spreading Lena Trough, Arctic Ocean. J. Petrol. 55, 427–458. https://doi.org/10.1093/petrology/egt073.

Lesher, C.E., 1990. Decoupling of chemical and isotopic exchange during magma mixing. Nature 344 (6263), 235–237.

Liang, Y., Schiemenz, A., Hesse, M.A., Parmentier, E.M., 2011. Waves, channels, and the preservation of chemical heterogeneities during melt migration in the mantle. Geophys. Res. Lett. 38, L20308. https://doi.org/10.1029/2011GL049034, 2011.

Ligi, M., Bonatti, E., Cipriani, A., Ottolini, L., 2005. Water-rich basalts at mid-ocean ridge cold spots. Nature 434, 66–69.

Liu, B., Liang, Y., 2017. The prevalence of kilometer-scale heterogeneity in the source region of MORB upper mantle. Sci. Adv. 3 (11) https://doi.org/10.1126/sciadv.1701872.

Liu, B., Liang, Y., 2019. Importance of permeability and deep channel network on the distribution of melt, fractionation of REE in abyssal peridotites, and U-series disequilibria in basalts beneath mid-ocean ridges: a numerical study using a 2D double-porosity model. Earth Planet. Sci. Lett. 528, 115788 https://doi.org/10.1016/j.epsl.2019.115788.

Liu, T., Wu, F.-Y., Liu, C.-Z., Eyuboglu, Y., Zhu, D.-C., Zhang, C., Ji, W.-B., Xu, Y., Zhang, Z.-Y., 2020. Testing oceanic crust–mantle decoupling by Sr–Nd–Hf–Os isotopes of Neo-Tethyan ophiolites. Lithos 376–377. https://doi.org/10.1016/j.lithos.2020.105757.

Longhi, J., 2002. Some phase equilibria systematics of lherzolite melting: I. Geochem. Geophys. Geosyst. 3, GC000204. https://doi.org/10.1029/2001GC000204.

Mallick, S., Dick, H.J.B., Sachi-Kocher, A., Salters, V.J., 2014. Isotope and trace element insights into heterogeneity of subridge mantle. Geochem. Geophys. Geosyst. 15, 2438–2453. https://doi.org/10.1002/2014gc005314.

Mallick, S., Standish, J.J., Bizimis, M., 2015. Constraints on the mantle mineralogy of an ultra-slow ridge: Hafnium isotopes in abyssal peridotites and basalts from the 9–25 E Southwest Indian Ridge. Earth Planet. Sci. Lett. 410, 42–532. https://doi.org/10.1016/j.epsl.2014.10.048.

Montanini, A., Tribuzio, R., Anczkiewicz, R., 2006. Exhumation history of a garnet pyroxenite-bearing mantle section from a continent–ocean transition (Northern Apennine Ophiolites, Italy). J. Petrol. 47, 1943–1971. https://doi.org/10.1093/petrology/egl032.

Piccardo, G.B., Zanetti, A., Müntener, O., 2007. Melt-peridotite interaction in the southern Lanzo peridotite: field, textural and geochemical evidence. Lithos 94, 181–209. https://doi.org/10.1016/j.lithos.2006.07.002.

Pushcharovsky, Yu.M., Raznitsin, Yu.N., Mazarovich, A.O., Skolotnev, S.G., Kepezinskas, P.K., Tyrko, N.N., Peyve, A.A., Dmitriev, D.A., 1992. Fracture zones Arkhangelsky, Doldrums and Vernadsky in the Central Atlantic: structure and rocks composition. Geotectonika 6, 63–79 (in Russian).

Python, M., Ceuleneer, G., 2003. Nature and distribution of dykes and related melt migration structures in the mantle section of the Oman ophiolite. Geochem. Geophys. Geosyst. 4, 8612. https://doi.org/10.1029/2002GC000354.

Rampone, E., Hofmann, A.W., 2012. A global overview of isotopic heterogeneities in the oceanic mantle. Lithos 148, 247–261. https://doi.org/10.1016/j.lithos.2012.06.018.

Rampone, E., Piccardo, G.B., Vannucci, R., Bottazzi, P., Ottolini, L., 1993. Subsolidus reactions monitored by trace element partitioning: the spinel- to plagioclase-facies transition in mantle peridotites. Contrib. Min. Petrol. 115, 1–17. https://doi.org/10.1007/BF00712974.

Rampone, E., Piccardo, G.B., Vannucci, R., Bottazzi, P., 1997. Chemistry and origin of trapped melts in ophiolitic peridotites. Geochim. Cosmochim. Acta 61, 4557–4569. https://doi.org/10.1016/S0016-7037(97)00260-3.

Rampone, E., Piccardo, G.B., Hofmann, A.W., 2008. Multistage melt–rock interaction in the Mt. Maggiore (Corsica, France) ophiolitic peridotites: microstructural and geochemical records. Contrib. Miner. Petrol. 156, 453–475. https://doi.org/10.1007/s00410-008-0296-y.

Rudge, J.F., Maclennan, J., Stracke, A., 2013. The geochemical consequences of mixing melts from a heterogeneous mantle. Geochim. Cosmochim. Acta 114, 112–143. https://doi.org/10.1016/j.gca.2013.03.042.

Salters, V.J.M., Dick, H.J.B., 2002. Mineralogy of the mid ocean ridge basalt source from neodymium isotopic composition of abyssal peridotites. Nature 418, 68–72. https://doi.org/10.1038/nature00798.

Salters, V.J.M., Stracke, A., 2004. Composition of the depleted mantle. Geochem., Geoph., Geosyst. 5, Q05B07. https://doi.org/10.1029/2003GC000597.

Salters, V.J.M., Zindler, A., 1995. Extreme $^{176}Hf/^{177}Hf$ in the sub-oceanic mantle. Earth Planet. Sci. Lett. 129, 13–30. https://doi.org/10.1016/0012-821X(94)00234-P.

Salters, V.J.M., Mallick, S., Hart, S.R., Langmuir, C.H., Stracke, A., 2011. Domains of depleted mantle; new evidence from hafnium and neodymium isotopes. Geochem., Geoph., Geosyst. 12, Q10017. https://doi.org/10.11029/12011GC003874.

Sanfilippo, A., Tribuzio, R., 2011. Melt transport and deformation history in a nonvolcanic ophiolitic section, northern Apennines, Italy: implications for crustal accretion at slow-spreading settings. Geochem. Geophys. Geosyst. 12, Q0AG04. https://doi.org/10.1029/2010G C003429.

Sanfilippo, A., Salters, V., Tribuzio, R., Zanetti, A., 2019. Role of ancient, ultra-depleted mantle in Mid-Ocean-Ridge magmatism. Earth Planet. Sci. Lett. 511, 89–98. https://doi.org/10.1016/j.epsl.2019.01.018.

Sanfilippo, A., Salters, V.J.M., Sokolov, S.Y., Peyve, A.A., Stracke, A., 2021. Ancient refractory asthenosphere revealed by mantle remelting at the Arctic Mid Atlantic Ridge. Earth Planet. Sci. Lett. 566, 116981 https://doi.org/10.1016/j.epsl.2021.116981.

Sanfilippo, A., Borghini, G., Guarnieri, L., Nakamura, E., Piccardo, G.B., Vannucci, R., Zanetti, A., 2022. A 400 Ma-long Nd-Hf isotopic evolution of melt-modified garnet-pyroxenites in an ancient subcontinental lithosphere (Lanzo North ophiolite, Western Alps). Chem. Geol. 588, 120643 https://doi.org/10.1016/j.chemgeo.2021.120643.

Sani, C., Sanfilippo, A., Ferrando, C., Peyve, A.A., Skolotonev, S.G., Muccini, F., Zanetti, A., Basch, V., Palmiotto, C., Bonatti, E., Ligi, M., 2020. Ultra-depleted melt refertilization of mantle peridotites in a large intra-transform domain (Doldrums Fracture Zone; 7–8°N, Mid Atlantic Ridge). Lithos 374, 105698. https://doi.org/10.1016/j.lithos.2020.105698.

Sani, C., Sanfilippo, A., Genske, F., Skolotnev, S., Ligi, M., Stracke, A., 2022. Mantle Re-Melting in an Intra-Transform Ridge Domain at the Doldrums Megatransform (Atlantic 7–8°N). Abstract at Goldschmidt conference, Hawaii, USA.

Sani, C., Sanfilippo, A., Peyve, A.A., Genske, F., Stracke, A., 2023. Earth mantle's isotopic record of progressive chemical depletion. AGU Advances 4. https://doi.org/10.1029/2022AV000792 e2022AV000792.

Seyler, M., Toplis, M.J., Lorand, J.P., Luguet, A., Cannat, M., 2001. Clinopyroxene microtextures reveal incompletely extracted melts in abyssal peridotites. Geology 29, 155–158. https://doi.org/10.1130/0091-7613(2001)029<0155:CMRIEM>2.0.CO;2.

Seyler, M., Lorand, J.-P., Dick, H.J.B., Drouin, M., 2007. Pervasive melt percolation reactions in ultra-depleted refractory harzburgites at the Mid-Atlantic Ridge, 15°-20°N: ODP Hole 1274A. Contrib. Min. Petrol. 153, 303–319. https://doi.org/10.1007/s00410-006-0148-6.

Shorttle, O., Maclennan, J., Lambart, S., 2014. Quantifying lithological variability in the mantle. Earth Planet. Sci. Lett. 395, 24–40. https://doi.org/10.1016/j.epsl.2014.03.040.

Skolotnev, S.G., Sanfilippo, A., Peyve, A.A., Muccini, F., Sokolov, S.Y., Sani, C., Dobroliubova, K.O., Ferrando, C., et al., 2020. Large-scale structure of the Doldrums multifault transform system (7-8°N Equatorial Atlantic): preliminary results from the 45th expedition of the R/V a.N Strakhov. Ofioliti 45, 25–41. https://doi.org/10.4454/ofioliti.v45i1.553.

Snow, J.E., 1993. The Isotope Geochemistry of Abyssal Peridotites and Related Rocks. Woods Hole Oceanographic Institution. Dept Of Applied Ocean Physics And Engineering.

Snow, J., Hart, S., Dick, H., 1994. Nd and Sr isotope evidence linking mid-ocean-ridge basalts and abyssal peridotites. Nature 371, 57–60. https://doi.org/10.1038/371057a0Sobolev.

Sobolev, A., Shimitzu, N., 1993. Ultra-depelted primary melt included in an olivine from the Mid-Atlantic Ridge. Nature 363, 153–154.

Stracke, A., 2012. Earth's heterogeneous mantle: a product of convection-driven interaction between crust and mantle. Chem. Geol. 330–331, 274–299. https://doi.org/10.1016/j.chemgeo.2012.08.007.

Stracke, A., 2021. A process-oriented approach to mantle geochemistry. Chem. Geol. 579, 120350 https://doi.org/10.1016/j.chemgeo.2021.120350.

Stracke, A., Bourdon, B., 2009. The importance of melt extraction for tracing mantle heterogeneity. Geochim. Cosmochim. Acta 73, 218–238. https://doi.org/10.1016/j.gca.2008.10.015.

Stracke, A., Zindler, A., Salters, V.J.M., McKenzie, D., Groenvold, K., 2003. The dynamics of melting beneath Theistareykir, northern Iceland. Geochem. Geophys. Geosyst. 4, 8513. https://doi.org/10.1029/2002GC000347.

Stracke, A., Snow, J.E., Hellebrand, E., von der Handt, A., Bourdon, B., Birbaum, K., Günther, D., 2011. Abyssal peridotite Hf isotopes identify extreme mantle depletion. Earth Planet. Sci. Lett. 308, 359–368. https://doi.org/10.1016/j.epsl.2011.06.012.

Stracke, A., Genske, F., Berndt, J., Koornneef, J.M., 2019. Ubiquitous ultra-depleted domains in Earth's mantle. Nat. Geosci. 12, 851–855. https://doi.org/10.1038/s41561-019-0446-z.

Suhr, G., Hellebrand, E., Snow, J.E., Seck, H.A., Hofmann, A.W., 2003. Significance of large, refractory dunite bodies in the upper mantle of the Bay of Islands Ophiolite. Geochem. Geophys. Geosyst. 4, 8605. https://doi.org/10.1029/2001GC000277.

Sun, S.-S., McDonough, W.F., 1989. Chemical and isotopic systematics of oceanic basalts: Implications for mantle composition and processes. In: Saunders, A.D., Norry, M.J. (Eds.), Magmatism in the Ocean Basins, vol. 42. Geol. Soc., London, pp. 313–345 (Special Publications).

Sun, C., Graff, M., Liang, Y., 2017. Trace element partitioning between plagioclase and silicate melt: the importance of temperature and plagioclase composition, with implications for terrestrial and lunar magmatism. Geochim. Cosmochim. Acta 206, 273–295. https://doi.org/10.1016/j.gca.2017.03.003.

Tackley, P.J., 2015. 7.12 - Mantle Geochemical Geodynamics. In: Schubert, G. (Ed.), Treatise on Geophysics. Elsevier, Oxford, pp. 521–585.

Tamura, A., Arai, S., Ishimaru, S., Andal, E.S., 2008. Petrology and geochemistry of peridotites from IODP Site U1309 at Atlantis Massif, MAR 30° N: micro- and macroscale melt penetrations into peridotites. Contrib. Mineral. Petrol. 155, 491–509. https://doi.org/10.1007/s00410-007-0254-0.

Tanaka, R., Makishima, A., Nakamura, E., 2008. Hawaiian double volcanic chain triggered by an episodic involvement of recycled material: Constraints from temporal Sr-Nd-Hf-Pb isotopic trend of the Loa-type volcanoes. Earth Planet. Sci. Lett. 265, 450–465.

Tartarotti, P., Susini, S., Nimis, P., Ottolini, L., 2002. Melt migration in the upper mantle along the Romanche Fracture Zone (Equatorial Atlantic). Lithos 63, 125–149. https://doi.org/10.1016/S0024-4937(02)00116-0.

Taylor, W.R., 1998. An experimental test of some geothermometer and geobarometer formulations for upper mantle peridotites with application to the thermobarometry of fertile lherzolite and garnet websterite. Neues Jahrbuch für Mineral Abh 172, 381–408.

Tilhac, R., Oliveira, B., Griffin, W.L., O'Reilly, S.Y., Schaefer, B.F., Alard, O., Ceuleneer, G., Afonso, J.C., Gr'egoire, M., 2020. Reworking of old continental lithosphere: Unradiogenic Os and decoupled Hf Nd isotopes in sub-arc mantle pyroxenites. Lithos 354–355. https://doi.org/10.1016/j.lithos.2019.105346.

Tilhac, R., Begg, G.C., O'Reilly, S.Y., Griffin, W.L., 2022. A global review of Hf-Nd isotopes: New perspectives on the chicken-and-egg problem of ancient mantle signatures. Chem. Geol. 609, 121039 https://doi.org/10.1016/j.chemgeo.2022.121039.

Tormey, D.R., Grove, T.L., Bryan, W.B., 1987. Experimental petrology of Normal MORB near the Kane Fracture Zone, 22-25°N. Mid-Atlantic Ridge. Contrib. Mineral. and Petrol. 96, 121–139. https://doi.org/10.1007/BF00375227.

Vernières, J., Godard, M., Bodinier, J.-L., 1997. A plate model for the simulation of trace element fractionation during partial melting and magma transport in the Earth's upper mantle. J. Geophys. Res. Solid Earth 102, 24771–24784.

Villiger, S., Ulmer, P., Müntener, O., Thompson, B., 2004. The liquid line of descent of anhydrous, mantle-derived, tholeiitic liquids by fractional and equilibrium crystallization - an experimental study at 1.0 GPa. J. Petrol. 45, 2369–2388. https://doi.org/10.1093/petrology/egh042.

Warren, J.M., 2016. Global variations in abyssal peridotite compositions. Lithos 248–251, 193–219. https://doi.org/10.1016/j.lithos.2015.12.023.

Warren, J.M., Shimizu, N., Sakaguchi, C., Dick, H.J.B., Nakamura, E., 2009. An assessment of upper mantle heterogeneity based on abyssal peridotite isotopic compositions. J. Geophys. Res. 114, B12203. https://doi.org/10.1029/2008JB006186.

Whattam, S.A., De Hoog, J.C.M., Leybourne, M.I., Khedr, M.Z., 2022. Link between melt-impregnation and metamorphism of Atlantis Massif peridotite (IODP Expedition 357). Contrib. Min. Petrol. 177, 106. https://doi.org/10.1007/s00410-022-01968-9.

White, W.M., 1985. Sources of oceanic basalts—radiogenic isotopic evidence. Geology 13, 115–118.Willig, M., Stracke, a., Beier, C., Salters, V. J., 2020. Constraints on mantle evolution from Ce-Nd-Hf isotope systematics. Geochim. Cosmochim. Acta 272, 36–53. https://doi.org/10.1016/j.gca.2019.12.029.

Witt-Eickschen, G., O'Neill, H.S.C., 2005. The effect of temperature on the equilibrium distribution of trace elements between clinopyroxene, orthopyroxene, olivine and spinel in upper mantle peridotite. Chem. Geol. 221, 65–101. https://doi.org/10.1016/j.chemgeo.2005.04.005.

Zhang, Z.Y., Liu, C.Z., Liang, Y., Zhang, C., Liu, T., Zhang, W.Q., Ji, W.B., 2022. Decoupled Trace Element and Isotope Compositions Recorded in Orthopyroxene and Clinopyroxene in Composite Pyroxenite Veins from the Xiugugabu Ophiolite (SW Tibet). J. Petrol. 63 (6) https://doi.org/10.1093/petrology/egac046.